APPLE: An Evolution Code for Modeling Giant Planets

Ankan Sur [ID],[1] Yubo Su [ID],[1] Roberto Tejada Arevalo [ID],[1] Yi-Xian Chen [ID],[1] and Adam Burrows [ID][1]

[1]*Department of Astrophysical Sciences, Princeton University, 4 Ivy Lane, Princeton, NJ 08544, USA*

ABSTRACT

We introduce APPLE, a novel planetary evolution code designed specifically for the study of giant exoplanet and Jovian planet evolution in the era of *Galileo*, *Juno*, and *Cassini*. With APPLE, state-of-the-art equations of state for hydrogen, helium, ice, and rock are integrated with advanced features to treat ice/rock cores and metals in the gaseous envelope; models for helium rain and hydrogen/helium immiscibility; detailed atmosphere boundary tables that also provide self-consistent albedos and spectra; and options to address envelope metal gradients and stably-stratified regions. Our hope is that these purpose-built features of APPLE will help catalyze the development of the next generation of giant exoplanet and Jovian planet evolutionary models.

Keywords: Planetary evolution — Exoplanets — Giant planets — Jupiter — Saturn

1. INTRODUCTION

The first giant exoplanet evolutionary models were created by Burrows et al. (1995). However, the characteristics of these models were informed by earlier evolutionary models of the Jovian planets of our solar system. Hence, they assumed adiabaticity, homogeneity, and simple atmospheres tied to interior adiabats (Hubbard 1968, 1969, 1977). Burrows et al. (1997), Baraffe et al. (1998), Burrows et al. (2001), and Baraffe et al. (2003) expanded upon this work with nongray atmospheric models as boundary conditions. From the outset, giant exoplanet evolutionary and spectral models were conceived in the context of a wider giant planet/brown dwarf continuum extending from ∼0.1 to ∼80 M_J (Jupiter mass). A more modern realization of this tradition with updated molecular opacities and atmospheres is the "Sonora-Bobcat" model suite of Marley et al. (2021). However, to date, such models generally still assume adiabaticity, lack heavy-element cores, do not incorporate helium rain (Stevenson & Salpeter 1977a), and assume homogeneity.

The early insights into Jovian planet properties were obtained by the *Voyager* (Hanel et al. 1981, 1983; Campbell & Synnott 1985) and *Pioneer* (Ingersoll et al. 1975) probes. These were followed by the *Galileo* entry probe (von Zahn & Hunten 1992; Niemann et al. 1992; Young et al. 1996), whose results have significantly enhanced our understanding of giant planet formation and evolution. In particular, *Galileo* provided estimates of Jupiter's atmospheric composition (generally ∼3×solar), but also indicated a depletion in atmospheric helium (to a mass fraction, Y, of ∼0.234) (von Zahn et al. 1998) compared to the protosolar value of ∼ 0.272[1] (Bahcall et al. 2006), hinting at the possibility of helium rain, as proposed by Stevenson & Salpeter (1977a,b) in the context of Saturn's "anomalous" luminosity. More recently, missions such as *Juno* (Bolton et al. 2017a,b) and *Cassini* (Spilker 2019) have measured the gravitational moments of Jupiter and Saturn (Iess et al. 2019; Durante et al. 2020), leading to the inference of chemically inhomogeneous models supporting the idea of an extended "fuzzy core" (Wahl et al. 2017; Debras & Chabrier 2019; Nettelmann et al. 2021; Militzer et al. 2022; Helled & Stevenson 2024). Moreover, *Cassini*, using Saturn ring seismology, suggests the presence in Saturn itself of g-mode oscillations and, hence, of a partially stably-stratified interior and dilute core there as well (Fuller 2014; Mankovich & Fuller 2021). These results for both Jupiter and Saturn highlight the limi-

Corresponding author: Ankan Sur
ankan.sur@princeton.edu

---

[1] This is the helium mass fraction, Y. Often, the helium abundance is given as $\frac{Y}{(1-Z)}$, where Z is the metallicity. Under this convention, which we do not follow, the initial value of $\frac{Y}{1-Z}$ is approximately 0.2777 (Bahcall et al. 2006).

tations of adiabatic modeling in the presence of composition gradients (Leconte & Chabrier 2012; Vazan et al. 2016; Berardo & Cumming 2017), as efficient convection would otherwise homogenize composition. They also punctuate the importance of more carefully addressing helium rain and hydrogen/helium immiscibility, as well as compositional inhomogeneity and non-adiabatic interiors.

Multiple research groups (Fortney & Hubbard 2003; Püstow et al. 2016; Mankovich et al. 2016; Mankovich & Fortney 2020) have recently addressed the challenge of hydrogen/helium immiscibility in Jupiter and Saturn by employing a variety of miscibility curves (e.g. Hubbard & Dewitt 1985; Pfaffenzeller et al. 1995; Lorenzen et al. 2011; Schöttler & Redmer 2018) and redistribution schemes. Most of these models were ad-hoc, some implemented by hand, and a more self-consistent treatment of helium rain coupled with modern immiscibility curves is now called for. Moreover, compositional inhomogeneity and non-adiabaticity may lead to stably-stratified layers in which doubly-diffusive (DD) (semi-)convection may be triggered (Rosenblum et al. 2011; Mirouh et al. 2012; Leconte & Chabrier 2012; Wood et al. 2013; Nettelmann et al. 2015). Energy transfer and compositional mixing within these layers would then be partially suppressed compared to overturning ("Ledoux") convection (Chabrier & Baraffe 1997; Leconte & Chabrier 2012, 2013), with implications for the evolution of a planet's luminosity and effective temperature ($T_{\rm eff}$). How to properly handle such physics in an evolutionary code has yet to be clearly determined (Vazan et al. 2015, 2016). Nettelmann et al. (2015) was the first to link Jupiter's thermal evolution with helium rain and DD convection while constraining the sizes of semi-convective layers to match its heat flux. This work has more recently been followed by Mankovich et al. (2016); Moll et al. (2016); Mankovich & Fortney (2020); and Fuentes et al. (2022). However, much work remains to be done to capture this effect with fidelity in an evolutionary context.

Furthermore, giant planet evolutionary calculations require careful consideration of atmospheric boundary conditions. Previous methodologies encompassed various approaches, including the non-gray isolated-object grid of model atmospheres by Burrows et al. (1997), the simpler model atmosphere grid proposed by Graboske et al. (1975), and the radiative-atmosphere grid presented by Fortney et al. (2011). Calculations often assume a Bond albedo and employ the approximate equation $T_{\rm eff}^4 = T_{\rm int}^4 + T_{\rm eq}^4$ (see e.g. Baraffe et al. 2003; Fortney & Hubbard 2003, 2004; Mankovich et al. 2016; Mankovich & Fortney 2020). Earlier models also overlooked the influence of cloud condensates in their at-

mospheres, which could significantly affect cooling. To address this, self-consistent model atmospheres, such as those developed by Chen et al. (2023), are needed. These models incorporate atmospheric radiative transfer, accommodate clouds of different particle sizes, and redistribute heat across day and night regions. They also implicitly provide geometric and Bond albedos, as well as emission spectra over a broad wavelength range.

Finally, another crucial facet of exoplanet and Jovian planet evolutionary modeling is the Equation of State (EOS) for the hydrogen and helium mixture. In the past, the SCvH95 EOS (Saumon et al. 1995) was used extensively in giant planet, giant exoplanet, and brown dwarf evolutionary codes (Burrows et al. 1997; Fortney & Hubbard 2003; Nettelmann et al. 2015; Mankovich et al. 2016). The default setting in the MESA (Paxton et al. 2011) stellar evolution code allows for the utilization of the SCvH95 EOS. However, with advancements in computational power and more sophisticated material physics techniques, a new generation of EOSes derived from ab initio simulations has become available (Nettelmann et al. 2008; Militzer et al. 2008; Nettelmann et al. 2012; Militzer & Hubbard 2013; Becker et al. 2014; Chabrier et al. 2019; Chabrier & Debras 2021). Although recent studies such as those of Püstow et al. (2016) and Mankovich & Fortney (2020) have adopted these EOSes, modern evolutionary tools should provide various EOS options within a unified framework.

Hence, recent discoveries by solar-system probes and improvements in the microphysics relevant to giant planet interiors highlight the need for new innovative approaches to giant planet evolutionary modeling. In addition, while current stellar evolution codes are sophisticated, they still face challenges in accurately simulating phenomena such as helium rain and in accommodating diverse EOSes and rocky cores. Furthermore, atmospheric physics for such codes, and for most codes used in the past to model giant planet evolution, remains rather limited. With these imperatives in mind, a new generation of evolution code is called for. In this spirit, we present here APPLE[2]. APPLE is a uniform modeling platform for giant exoplanet and Jovian planet evolutionary simulations. In this paper, we explain its architecture, the numerical techniques employed, and the physical principles that undergird it. The versatility of APPLE is showcased through a series of test cases, illustrating its application across a range of planetary conditions and scenarios. The structure of APPLE is modular

---

[2] which stands for A Python code for PLanetary Evolution

and its computational structure easily enables upgrades as new physics and techniques appear.

This paper is organized as follows. §2 provides the structure and evolution equations, while §3 discusses the associated boundary conditions. §4 explains the physics of energy transport in planetary interiors and §5 discusses the mixing and diffusion of elements. We continue a discussion of the relevant microphysics in §6 and in §7 we describe the model atmosphere approach for giant planets we employ. This methodology also provides albedos and emission spectra (Chen et al. 2023). We then go on in §8 to discuss the computation methods used in APPLE and in §9 present example simulations. The full numerical scheme, including the finite difference and discretization procedures, is presented in the Appendix. A list of symbols with their definitions is presented in Table 1. We wrap things up in §10 with a summary discussion and thoughts on future directions.

2. STRUCTURE AND EVOLUTION EQUATIONS

The equations that describe the evolution of planets parallel those employed in stellar evolution (Eggleton 1971; Demarque et al. 2008; Christensen-Dalsgaard 2008; Weiss & Schlattl 2008; Morel & Lebreton 2008; Christensen-Dalsgaard 2008; Paxton et al. 2011, 2013, 2018, 2019) which are the equations of mass, momentum, energy, and species conservation. Dropping the acceleration (inertia) term in the momentum equation, assuming that transport of energy and species are diffusive processes, and assuming spherical symmetry, one arrives at a standard set of coupled differential equations:

$$\frac{dP}{dM_r} = -\frac{GM_r}{4\pi r^4} + \frac{\Omega^2}{6\pi r} \tag{1}$$

$$\frac{dr}{dM_r} = \frac{1}{4\pi r^2 \rho} \tag{2}$$

$$\frac{\partial L}{\partial M_r} = -\frac{dU}{dt} - P\frac{d(\frac{1}{\rho})}{dt} \tag{3}$$

$$= -T\frac{dS}{dt} - \sum_i \left(\frac{\partial U}{\partial X_i}\right)_{s,\rho} \frac{dX_i}{dt} \tag{4}$$

$$N_A \frac{dX_i}{dt} = -\frac{\partial}{\partial M_r}\left(4\pi r^2 F_i\right), \tag{5}$$

where M_r is the independent Lagrangian coordinate denoting the mass enclosed in a sphere of radius r, P is the pressure, $L = 4\pi r^2 \mathcal{F}$ is the luminosity, $\mathcal{F}$ is the energy flux, S is the specific entropy, ρ is the mass density, and T is the temperature, U is the specific internal energy, N_A is Avogardo's number, and X_i is the mass fraction of species i. Note that these equations involve the specific quantities (e.g., per gram), not the per volume quantities. To approximately incorporate the possible angle-averaged structural effects of solid-body rotation (with angular frequency Ω), we follow Kippenhahn et al. (2013) in introducing an additional term in eq. 1. For our purposes, $X_i = \{X, Y, Z\}$, where X, Y, and Z are the mass fractions of hydrogen, helium, and heavy elements, respectively, and $\sum X_i = 1$. The formalism can easily be extended to follow multiple heavy species. F_i is the flux of species i (and has both diffusive and advective contributions) and will be discussed in the context of helium rain in §5 and §5.4. We note that, as is standard practice in spherical stellar and planetary evolution, we treat mixing processes using an equation with a diffusive form. This allows one to conserve the mass in a species to machine precision by differencing it using Gauss's theorem. A similar approach is followed for Z mixing, but for brevity is not highlighted in this paper.

We note that $\frac{\partial U}{\partial X_i}$ is directly related to the chemical potential (μ_i), modulo Avogadro's number, and that there are two ways of writing the energy conservation equations eq. 3 and eq. 4. Equation 3 is the standard statement of energy conservation that explicitly focuses on the change in internal energy (temperature) and the work done ("PdV"). The other focuses explicitly on the entropy change and composition changes. For adiabatic and fully convective behaviors, the latter is more natural and represents the early history of the field when giant planets were thought to be fully convective and the second term was finessed (Fortney & Hubbard 2003; Mankovich & Fortney 2020). However, the *Juno* and *Cassini* data now strongly suggest that such pioneering models have seen their day and that composition gradients and changes in X_i with time (such as accompanying helium rain and heavy element redistribution) must be incorporated. In APPLE, we employ the approach summarized with eq. 4. We were motivated to use entropy, composition, and density/radius as our primary variables in our Lagrangian code by the continuing importance of convection and convective energy and species transport and map out our computational methodology in §8.

Since we focus on Jovian planets, which are primarily composed of hydrogen and helium, along with some fraction of heavy elements distributed in the core and the envelope, we must use radiative opacities and conductivities (described in §4.1), an algorithm for handling convective energy transport (described in §4.2), an approach to species mixing (described in §5), hydrogen-helium and metal equations of state (described in §6.1), and, importantly, a methodology for incorporating the atmosphere boundary conditions that drive the global

evolution of the entire system (described in §7). `APPLE` has been constructed with multiple embedded sets of microphysical inputs and has been made modular and flexible to accommodate upgrades in the input physics as they arise.

3. BOUNDARY CONDITIONS

The two hydrostatic equilibrium equations 1 and 2 need two boundary conditions to be solved, namely, one for pressure and the other for the radius. Ideally, the outer pressure should be zero, and we set it to a very small number (for numerical convenience) compared to the interior pressures. Therefore, we have

$$P_{\text{surf}}(M_r = M_p) = \text{"1 bar"} \tag{6}$$
$$r_{\text{center}}(M_r = 0) = 0, \tag{7}$$

where M_p is the total mass of the planet. To solve the evolution equations 3 and 4, four boundary conditions must be met. For energy transport, at the outer boundary, the surface flux is given by

$$\mathcal{F}_{\text{surf}} = 4\pi R_p^2 \sigma T_{\text{int}}^4, \tag{8}$$

where the internal temperature, T_{int}, is calculated using a sophisticated atmospheric model as a function of gravity and entropy (see §7), and R_p is the planet's radius at a given age. At the inner boundary, we set

$$\mathcal{F}_{\text{center}}(M_r = 0) = 0. \tag{9}$$

Both at the core-envelope boundary and at the surface, we use zero flux boundary conditions for the diffusion equation 5. This is achieved by setting the diffusion coefficient at the boundaries equal to

$$4\pi r^2 \rho \mathcal{D} \frac{\partial Y}{\partial r} \bigg|_{M_r = M_c} = 4\pi r^2 \rho \mathcal{D} \frac{\partial Y}{\partial r} \bigg|_{M_r = M_p} = 0, \quad (10)$$

where M_c is the mass coordinate at the envelope-core boundary, interior to which resides the "ice/rock" core (of flexible composition), and $\mathcal{D}$ is the relevant diffusivity parameter. If there is no core, $M_c = 0$.

4. ENERGY TRANSPORT

4.1. *Radiation and Conduction*

A planet's structure and evolution are profoundly influenced by the mechanisms of heat transfer within their interiors and atmospheres (Stevenson 1982; Burrows et al. 1997; Marley et al. 1999; Hubbard et al. 1999; Burrows et al. 2001; Fortney & Hubbard 2003; Fortney et al. 2011; Mankovich et al. 2016). Conduction and radiation are basic processes that can play a key, though often subdominant, role.

Symbol	Meaning
a	Radiation constant
c	Speed of light
C_p	Specific heat at constant pressure
C_v	Specific heat at constant volume
$\mathcal{D}_{\text{MLT}}$	Diffusion coefficient set by MLT
$\mathcal{D}_{\text{micro}}$	Microscopic diffusion coefficients
$\mathcal{D}_{\text{sc}}$	Semiconvective diffusion coefficients
$\mathcal{F}$	Energy flux
g	Acceleration due to gravity
G	Universal Gravitation constant
H_p	Pressure scale height
$H_r, \mathcal{H}_r$	Helium rain scale parameters
k_B	Boltzmann constant
κ_R	Rosseland mean opacity
L	Luminosity
λ_{cd}	Thermal conductivity due to conduction
λ_r	Thermal conductivity due to radiation
M_r	Mass enclosed at radius r
M_p	Mass of the planet
Nu_T	Thermal Nusselt number
Nu_X	Compositional Nusselt number
∇	$\equiv \frac{d \ln T}{d \ln P}$, Temperature gradient
∇_{ad}	$\equiv \frac{\partial \ln T}{\partial \ln P}\big|_S$, Adiabatic temperature gradient
Ω	Angular frequency
P	Pressure
Pr	Prandlt number
ρ	Density
r	Radial coordinate
R_ρ, R_0	Density ratio in semiconvection
Ra_T	Rayleigh number
R_p	Radius of the planet
σ	Stefan-Boltzmann constant
S	Specific entropy
T	Temperature
T_{int}	Internal/Intrinsic temperature
T_{eff}	Effective temperature
τ	Lewis number
U	Specific internal energy
μ_i	Chemical potential of species i
v_{MLT}	Velocity of a fluid parcel from MLT
χ_T	$\equiv -\frac{\partial \ln P}{\partial \ln T}\big|_{\rho, Y}$
χ_Y	$\equiv \frac{\partial \ln P}{\partial Y}\big|_{\rho, T}$
X	Mass fraction of hydrogen
Y	Mass fraction of helium
Y_{atm}	Atmospheric helium abundance
Y_{misc}	Immiscibility Helium fraction
Z	Mass fraction of heavy elements

Table 1. Some useful symbols used in this paper and the `APPLE` code.
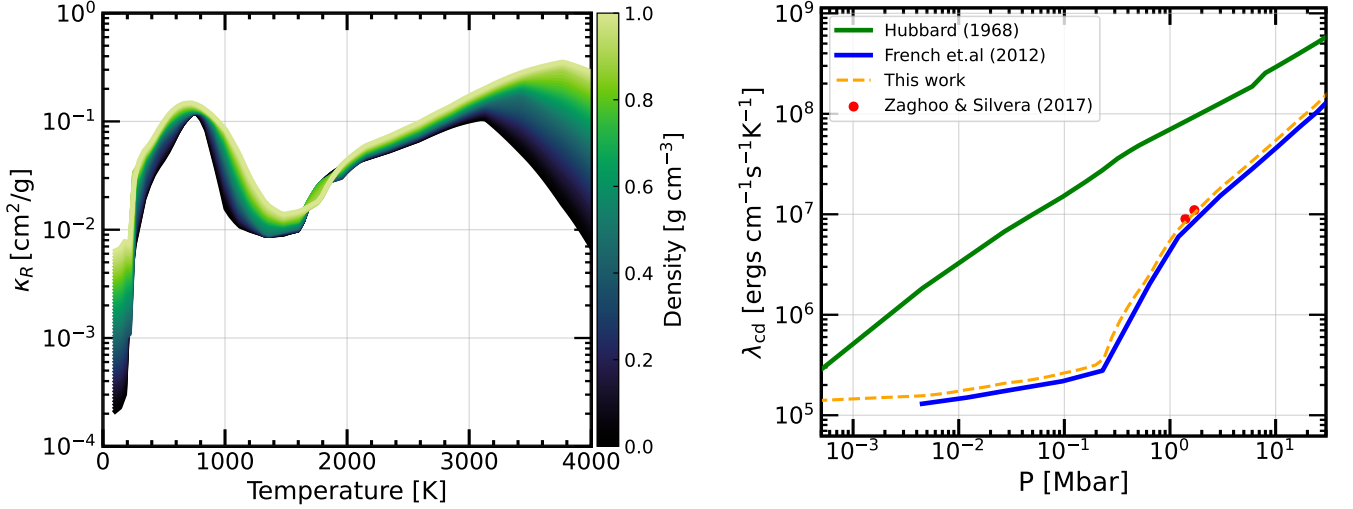
Figure 1. Left panel: Variation of Rosseland Mean Opacities (κ_R) with temperature and density. Right panel: Thermal conductivity λ_{cd} as a function of pressure. The green line represents the result obtained from (Hubbard 1968), whereas the blue line represents the result obtained from French et al. (2012). The red dots are experimental values obtained by (Zaghoo & Silvera 2017). We use the functional form of French et al. (2012), multiplying it by 1.2 to match the experimental values.

Radiative transfer is an important mode of energy transport in stars and in the outer layers of planets (Hubbard 1968; Guillot et al. 1994b,a, 1995; Chabrier & Baraffe 1997; Arras & Bildsten 2006; Robinson & Catling 2012). In the context of stellar and planetary evolution, radiation is treated as a diffusive process. The radiative flux is given by Kippenhahn & Weigert (1990):

$$\mathcal{F}_r = -\frac{4ac}{3}\frac{T^3}{\kappa_r \rho}\frac{\partial T}{\partial r} = -\lambda_r \frac{\partial T}{\partial r}, \qquad (11)$$

where κ_r is the Rosseland mean coefficient and $\lambda_r = \frac{4ac}{3}\frac{T^3}{\kappa_r \rho}$ is the associated "thermal conductivity". In APPLE, we adhere to a conventional approach wherein we delineate the absorption characteristics and bound-bound transitions of atoms and molecules through precalculated, fixed tables containing Rosseland mean opacities, denoted as $\kappa_R(\rho, T)$ from Sharp & Burrows (2007) and updated recently by Lacy & Burrows (2023), but the code can accommodate any opacity tables. The table spans a temperature range between $100 \le T \le 4000$ K while the density range is $10^{-5} \le \rho \le 10^{-2}$ g cm^{-3}. The left panel of Figure 1 shows κ_R as a function of ρ and T. We note that it is only in the atmosphere that such transport is generally relevant to planetary evolution and that we already precalculate and tabulate a set of atmosphere boundary conditions to determine the total energy flux out of the planet and the outer flux boundary condition (see §7 and §3). Nevertheless, including a radiative flux capability in the numerics is not double counting and allows us to incorporate radiative transfer effects in the inner regions, should they become of importance.

Another mechanism of heat transfer in planetary interiors is conduction. This mode of energy transport is particularly important inside a planet's "rocky" core (see Labrosse 2015, for a detailed discussion), is generally more important than radiative transfer (except in the atmosphere), but is far less effective in transporting heat than convection (§4.2) or semiconvection (§4.3). The rate of conductive heat transfer is dictated by the temperature gradient and the material properties. The heat flux due to conduction is given by:

$$\mathcal{F}_{cd} = -\lambda_{cd}\frac{dT}{dr}, \qquad (12)$$

where λ_{cd} is the thermal conductivity of the material in question.

Conduction via electron transport is important at higher pressures, though in the traditional energy transport model in giant planets, it is subdominant. Nevertheless, we include it for completeness and may find a role in some contexts. Hubbard (1968) estimated the thermal conductivity as

$$\lambda_{cd} \sim 10^8 \left(\frac{\rho}{1\,\mathrm{g\,cm^{-3}}}\right)^{4/3} \mathrm{ergs\,cm^{-1}\,s^{-1}\,K^{-1}}. \qquad (13)$$

The dependence of λ_{cd} on the helium abundance is relatively small (but see Preising et al. (2023)). This research is somewhat dated as our understanding of the equations of state and material properties has significantly advanced since then. French et al. (2012) carried out more refined calculations of material properties

using ab initio molecular dynamics simulations, focusing on a hydrogen-helium-water mixture along Jupiter's supposed adiabat. They found that the thermal conductivity is predominantly electron-dominated in the metallic region, but decreases strongly at the transition zone to the molecular phase, where ionic contributions begin to dominate. This behavior is summarized in the right panel of Figure 1 as a function of pressure.

Calculations by French et al. (2012) are based on Density Functional Theory, which slightly underestimates conduction when compared to liquid metallic hydrogen experiments (Zaghoo & Silvera 2017), as shown by the red dots in Figure 1. However, this value is lower than theoretical estimates used in heat-transport models for Jovian-like planets (Hubbard 1968; Stevenson & Salpeter 1977a; Potekhin 1999). We use a linear interpolation on the French et al. (2012) data, multiplied by 1.2 to match the experimental value, shown by the orange-dashed line in Figure 1. We also extrapolate linearly the thermal conductivity over logarithmic pressure scales at regions outside the French et al. (2012) table. The recent sophisticated calculations by Preising et al. (2023) for helium-rich conditions that might prevail in Saturn's interior are also available as an option for the thermal diffusivities employed in APPLE.

4.2. Convection

Convection is still at present, the dominant energy and species transport mechanism in planetary atmospheres and interiors. One of the most widely applied models for handling this complicated three-dimensional and turbulent process in a simplified spherical context is Mixing Length Theory (MLT) (Böhm-Vitense 1958). According to MLT, heat is transported by thermal parcels over characteristic length scales before dispersing into the surrounding fluid. The mixing length describes the average vertical distance traveled before a convective fluid element becomes thermally equilibrated with its surroundings. While the theory doesn't explicitly define this mixing length, it is commonly expressed in terms of the local pressure scale height ($H_p = -\frac{dr}{d \ln P}$), and is defined as $l = \alpha H_p$, where α is a tunable constant (which we generally set equal to 1).

The convective flux in the MLT is conceptualized as the excess energy carried by a convective parcel, multiplied by its velocity. Mathematically, this is expressed as

$$\mathcal{F}_{\mathrm{conv}} = \rho v_{\mathrm{MLT}} C_p \Delta T \,, \tag{14}$$

where v_{MLT} is its velocity, C_p is the specific heat at constant pressure, and ΔT is the temperature difference between the fluid element and its environment. Under the assumption of small adiabaticity, the temperature

variation can be expressed as

$$\Delta T = \left[-\left(\frac{dT}{dr}\right) + \left(\frac{dT}{dr}\right)_{\mathrm{ad}} \right] \Delta r \tag{15}$$

$$= (\nabla - \nabla_{\mathrm{ad}}) \frac{l}{2} \frac{T}{H_p} \,, \tag{16}$$

where $\nabla = \frac{d \ln T}{d \ln P}$ and $\nabla_{\mathrm{ad}} = \frac{\partial \ln T}{\partial \ln P}\big|_S$. We assume the average distance traveled by a fluid element before mixing with its surroundings is $\Delta r = l/2$. The average velocity of the fluid element can then be calculated as (Kippenhahn & Weigert 1990):

$$v_{\mathrm{MLT}}^2 = g(\nabla - \nabla_{\mathrm{ad}}) \frac{l^2}{8 H_p} \,. \tag{17}$$

In the absence of composition gradients, we can express the temperature gradients in terms of the entropy (S) gradient as

$$\frac{dT}{dr} = \frac{\partial T}{\partial P}\bigg|_S \frac{dP}{dr} + \frac{\partial T}{\partial S}\bigg|_P \frac{dS}{dr} \tag{18}$$

$$= \frac{dT}{dr}\bigg|_{\mathrm{ad}} + \frac{T}{C_p} \frac{dS}{dr} \tag{19}$$

Employing the definition of H_p in equation 19, we get

$$\nabla - \nabla_{\mathrm{ad}} = -\frac{dS}{dr} \frac{H_p}{C_p} \,. \tag{20}$$

The Schwarzschild criterion for convection (Schwarzschild & Härm 1958) is given by

$$\nabla - \nabla_{\mathrm{ad}} > 0 \tag{21}$$

and the corresponding convective flux[3] is (Tejada Arevalo et al. 2024):

$$\mathcal{F}_{\mathrm{conv}} = \rho T \sqrt{\frac{g l^4}{32 C_p}} \left(\left[-\frac{dS}{dr} + \left(\frac{\partial S}{\partial Y}\right)_{P,T} \frac{dY}{dr} \right]_+ \right)^{3/2} . \tag{22}$$

However, if there is a composition gradient in the medium, the convective criterion is given by the Ledoux condition (Ledoux 1947)

$$\nabla - \nabla_{\mathrm{ad}} - \frac{\chi_Y}{\chi_T} \frac{dY}{d \log P} > 0 \tag{23}$$

$$\implies \frac{dS}{dr} - \left(\frac{\partial S}{\partial Y}\right)_{P,\rho} \frac{dY}{dr} < 0 \,, \tag{24}$$

---

[3] Note that, even though there is the dY/dr term in the convective flux using the Schwarzschild criterion, the term in the bracket equals $\nabla - \nabla_{\mathrm{ad}}$. Also, the $+$ indicates that only the positive value of the expression is used in the square bracket, otherwise, it is zero.

where $\chi_Y = \left(\frac{\partial \ln P}{\partial Y}\right)_{\rho,T}$, and $\chi_T = -\left(\frac{\partial \ln P}{\partial \ln T}\right)_{\rho,Y}$. The corresponding flux is approximated as

$$\mathcal{F}_{\text{conv}} = \rho T \sqrt{\frac{gl^4}{32 C_p}} \left(\left[-\frac{dS}{dr} + \left(\frac{\partial S}{\partial Y}\right)_{P,\rho} \frac{dY}{dr}\right]_+\right)^{3/2}, \tag{25}$$

where we have generalized the flux here consistently to comport with the Brunt (Kippenhahn & Weigert 1990) associated with the Ledoux condition, rather than the Brunt associated with the Schwarzschild condition. Numerically, we set $\mathcal{F}_{\text{conv}} = v_{\text{MLT}} = 0$ when a mass zone is stable to convection.

Semiconvection has often been modeled (Leconte & Chabrier 2012; Mirouh et al. 2012) by introducing a parameter R_ρ, often referred to as the "density ratio." In general, we may introduce a coefficient to the $\frac{dY}{dr}$ term in the convective flux:

$$\frac{\partial S}{\partial Y} = (1 - R_\rho)\left(\frac{\partial S}{\partial Y}\right)_{P,T} + R_\rho \left(\frac{\partial S}{\partial Y}\right)_{P,\rho}, \tag{26}$$

such that the following criterion holds:

$$R_\rho = \begin{cases} 0 & \text{Schwarzschild}, \\ 1 & \text{Ledoux}, \\ > 0 \text{ but} < 1 & \text{"pseudo"-semiconvection}, \end{cases} \tag{27}$$

and we can mimic the thermal effect of semiconvection by varying R_ρ (see Mankovich et al. 2016). However, this effectively just shows how convection might vary between Ledoux and Schwarzschild and is not a good substitute for a more physical theory of semiconvection.

4.3. Semiconvection

Semiconvective heat transport is expected to occur in regions unstable to the Schwarzschild criterion but stable to the Ledoux criterion. Parameters said to govern energy transport in a semiconvective region (Walin 1964; Kato 1966) are the Prandlt number (Pr), the diffusivity ratio (τ, also called the "Lewis number"), and the density ratio (R_0), respectively, each defined as

$$\text{Pr} \equiv \frac{\nu}{\kappa_T}, \tag{28}$$

$$\tau = \frac{\mathcal{D}}{\kappa_T}, \tag{29}$$

$$R_0 = \frac{\delta}{\phi}\left(\frac{\nabla - \nabla_a}{\nabla_Y}\right), \tag{30}$$

where κ_T and $\mathcal{D}$ are the thermal and compositional diffusivities, ν is the viscosity, ∇_Y is derived using eq. 24, and

$$\delta = \left(\frac{\partial \log \rho}{\partial \log T}\right)_{P,Y}, \quad \phi = \left(\frac{\partial \log \rho}{\partial \log Y}\right)_{P,T}, \tag{31}$$

$$\nabla = \frac{d \log T}{d \log T}, \text{ and } \nabla_a = \left(\frac{\partial \log T}{\partial \log P}\right)_{S,Y}. \tag{32}$$

In the context of giant planet envelopes dominated by hydrogen/helium mixtures, Pr and τ are approximately equal to $\sim 10^{-2}$. Semiconvection occurs when $R_c < R_0 < 1$ (Walin 1964; Kato 1966), where

$$R_c = \frac{\text{Pr} + \tau}{\text{Pr} + 1}. \tag{33}$$

Regions where $1 > R_0 > R_c$ are unstable to semiconvection. Note that $R_0 = 0$ is the Schwarzschild condition and $R_0 = 1$ is the Ledoux condition.

Several important studies of semiconvection in the regime relevant to giant planets have been conducted (Rosenblum et al. 2011; Mirouh et al. 2012; Wood et al. 2013; Moll et al. 2016). These authors explored the onset of semiconvection (Rosenblum et al. 2011; Wood et al. 2013) which, though less efficient than full convection, nevertheless transports heat and mix matter through layered regions (Mirouh et al. 2012; Moll et al. 2016).

APPLE implements the empirical relations found by Mirouh et al. (2012) and Wood et al. (2013) to control the transport of heat and composition in semiconvective regions via the thermal and compositional Nusselt numbers, Nu_T and Nu_X. In the case of non-layered convection, Mirouh et al. (2012) found that

$$\text{Nu}_T - 1 \approx 0.75 \left(\frac{\text{Pr}}{\tau}\right)^{0.25 \pm 0.15} \frac{1 - \tau}{R_0^{-1} - 1}\left(1 - \frac{R_0^{-1} - 1}{R_c^{-1} - 1}\right). \tag{34}$$

In the case of layered convection, Wood et al. (2013) found that Nu_T and Nu_X can be approximated via empirical relations,

$$\text{Nu}_T - 1 = A_T \text{Ra}_T^a \text{Pr}^b \tag{35}$$

$$\text{Nu}_X - 1 = A_X \tau^{-1} \text{Ra}_T^c \text{Pr}^d, \tag{36}$$

where $A_T \approx 0.1$, $A_X \approx 0.03$, $a = 0.34 \pm 0.01$, $b = 0.34 \pm 0.03$, $c = 0.37 \pm 0.01$, and $d = 0.27 \pm 0.04$ (Wood et al. 2013; Moll et al. 2016). The parameter Ra_T is the same modified Rayleigh number parameter used in stellar and planetary semiconvection studies (Leconte & Chabrier 2012; Spruit 2013; Zaussinger & Spruit 2013; Wood et al. 2013; Nettelmann et al. 2015; Moore & Garaud 2016),

$$\text{Ra}_T = \frac{\alpha g l_H^4}{\kappa_T \nu}\left(\frac{dT}{dr} - \frac{dT_{\text{ad}}}{dr}\right). \tag{37}$$

In lieu of any exact knowledge of the various parameters on which the Nusselt numbers depend, APPLE employs empirical relations with constant values of $\mathrm{Pr} = 0.01$ and $\tau = 0.01$. This simplifies the expression for the thermal Nusselt number found by Mirouh et al. (2012) to

$$\mathrm{Nu}_T \approx \frac{0.74}{\mathrm{R}_0^{-1} - 1} + 0.85 \qquad (38)$$

and if $c = 0.37$, $d = 0.27$, then the empirical relations of Nu_T and Nu_X found by Wood et al. (2013) become

$$\mathrm{Nu}_T \approx 0.02\,\mathrm{Ra}_T(\mathrm{l_H})^{0.34} + 1 \qquad (39)$$

$$\mathrm{Nu}_X \approx 0.86\,\mathrm{Ra}_T(\mathrm{l_H})^{0.37} + 1. \qquad (40)$$

However, APPLE can vary such Nusselt values in semiconvective layers. The thermal Nusselt number is used to modify the heat flux due to conduction and is given by

$$\mathcal{F}_s = -\lambda_{\mathrm{cd}}(\mathrm{Nu}_T - 1)\left[\frac{dT}{dr} - \frac{dT}{dr}\bigg|_{\mathrm{ad}}\right] \qquad (41)$$

$$= -(\mathrm{Nu}_T - 1)\frac{\lambda_{\mathrm{cd}}T}{C_P}\left[\frac{dS}{dr} - \left(\frac{\partial S}{\partial Y}\right)_{P,T}\frac{dY}{dr}\right] \qquad (42)$$

so that the total flux in semiconvective regions becomes

$$\mathcal{F}_{\mathrm{tot}} = \mathcal{F}_{\mathrm{cd}} + \mathcal{F}_s = -\lambda_{\mathrm{cd}}\left[\frac{dT}{dr} + (\mathrm{Nu}_T - 1)\left(\frac{dT}{dr} - \frac{dT}{dr}\bigg|_{\mathrm{ad}}\right)\right]$$
$$= -\lambda_{\mathrm{cd}}\left[\frac{dT}{dr} + (\mathrm{Nu}_T - 1)\frac{T}{C_P}\left[\frac{dS}{dr} - \left(\frac{\partial S}{\partial Y}\right)_{P,T}\frac{dY}{dr}\right]\right]. \qquad (43)$$

5. MIXING/DIFFUSION OF ELEMENTS

The distribution of heavy elements plays a crucial role in understanding the formation and origin of the planets (Helled & Lunine 2014; Helled et al. 2022). Moreover, the mixing of chemical species by convection, microscopic diffusion, or phase separation (such as in helium rain) are important global processes to follow during a giant planet's evolution. However, particularly in the case of phase separation and helium rain, the proper numerical approach to incorporate with some fidelity such multi-fluid/multi-phase physics into a spherical code is not yet clear. Presently, there are no cogent models of helium bubble growth, and in the case of non-convective mixing, a compelling model of droplet upwelling and settling (Fortney & Hubbard 2003; Püstow et al. 2016; Mankovich et al. 2016). Therefore, in lieu of this, we have introduced an advective term into the general diffusion equation for a species such as helium that can

phase-separate and rain. This establishes for raining species such as helium an asymptotic equilibrium scale, akin to a cloud deck, that captures the rain region in a manner consistent with the physical miscibility curves employed. In this spirit, we have crafted two schemes, both of which are fully consistent with whichever miscibility model is employed, and we describe them in §5.4. Next, we discuss the different types of mixing and their associated diffusion coefficients.

5.1. Convective Mixing

When convection is generally dominant in the interior such a region mixes matter very rapidly compared with evolutionary timescales (e.g., Kelvin-Helmholtz timescales). Given this, the chemical profile in convective layers can generally quickly flatten. To accomplish this naturally for the evolution of any mass fraction $X_i = \{X, Y, Z\}$, we employ in such convective regions a diffusion equation:

$$\frac{dX_i}{dt} = \frac{\partial}{\partial M_r}\left(4\pi r^2 \rho \mathcal{D}\frac{\partial X_i}{\partial r}\right), \qquad (44)$$

with the diffusion coefficient assumed to have the form

$$\mathcal{D} = \mathcal{D}_{\mathrm{MLT}} = \frac{1}{3}v_{\mathrm{MLT}}l, \qquad (45)$$

where v_{MLT} is given by equation 17 and l is the effective "mean-free-path" for tubules, in this formulation set equal to the local mixing length. We note that this equation is non-linear since $\mathcal{D} \propto v_{\mathrm{MLT}}$, and is a complicated function of thermal profiles and thermodynamic quantities (§4.2).

5.2. Semiconvective Mixing

The transport of elements in a semiconvective region is governed by the compositional Nusslet number, Nu_X. The Nusselt number will enhance a diffusion coefficient, $\mathcal{D}$ such that the semiconvective effective diffusion coefficient is $\mathcal{D}_{\mathrm{sc}} = \mathrm{Nu}_X\mathcal{D}$. The diffusion equation through a semiconvective layer is therefore

$$\frac{dX_i}{dt} = \frac{\partial}{\partial M_r}\left(4\pi r^2 \rho \mathcal{D}_{\mathrm{sc}}\frac{\partial X_i}{\partial r}\right), \qquad (46)$$

where Nu_X is either taken from the empirical relation of Wood et al. (2013) or left as a free parameter.

5.3. Microscopic Diffusion

Within quiescent regions, microscopic diffusion is generally slow and the associated diffusivities are small. In stars, gravitational settling proceeds at a glacial pace

and has been studied quantitatively and in-depth for many decades. The mass fraction of helium (Y) in the Sun's atmosphere has taken its long lifetime to be depleted from ∼0.2725 to only ∼0.245 (Peimbert et al. 2007). Nevertheless, this estimated primordial helium abundance is now compared with the *Galileo* measurement of Y_{atm} ∼0.234 in Jupiter's atmosphere (von Zahn et al. 1998) to infer that there has been helium rainout even in Jupiter. To address this phenomenon, we have developed a set of schemes in a time-dependent and evolutionary context that, while not the final word, provides a useful and informative modeling context and methodology. When convection, semiconvection, and/or rain are not operative, we use a microscopic diffusivity, $\mathcal{D}_{micro}$, that generally would result in a long diffusion timescale of order 1 Gyr across the whole planet, if dominant. We now proceed to a discussion of our algorithms for handling helium rain with an advective-diffusive algorithm.

5.4. *Helium Rain*

Hydrogen-helium immiscibility was initially proposed to explain Saturn's luminosity excess by Stevenson & Salpeter (1977a). The settling of helium in the gravitational well would translate into the heating of the gas. A gradual removal of helium from the planet's outer layer would occur in the immiscibility layer as helium droplets formed and rained down into the deeper interior. Recent theoretical miscibility diagrams for hydrogen/helium mixtures (Lorenzen et al. 2011; Morales et al. 2009; Schöttler & Redmer 2018) at Megabar (Mbar) pressures generally support this possibility, though these miscibility theories disagree in detail (§6.2). To address this physics in an evolutionary code, we have developed two related, but different, approaches to handling it.

5.4.1. *Scheme A*

In this framework, we model the helium rain as an advection/diffusion process and assume the same diffusion coefficient as pertains locally to any other species. Importantly, we use realistic hydrogen-helium phase diagrams (in $P-T$ space) and identify the region(s) at any given time where the planetary pressure-temperature profile intersects the miscibility curve. Within the planet, the intersection results in two pressure points, P_1 and P_2, where the helium phase separates and rains. P_1 represents the outermost pressure of immiscibility, whereas P_2 denotes the innermost pressure of immiscibility. The absence of P_1 results in no rainfall, whereas in the absence of P_2, we utilize the innermost pressure within the gaseous envelope. Therefore, the diffusion equation is modified to include an extra advective term for helium settling. In a convective region, we have:

$$\frac{dY}{dt} = \frac{\partial}{\partial M_r}\left\{4\pi r^2 \rho \left(\mathcal{D}_{MLT}\frac{\partial Y}{\partial r} + \bar{D}\frac{Y}{H_r}\right)\right\}, \quad (47)$$

where H_r is an arbitrary scale parameter and

$$\bar{D} = \begin{cases} \mathcal{D}_{MLT} & \text{if } P_1 \leq P \leq P_2 \\ 0 & \text{otherwise}. \end{cases} \quad (48)$$

Notice that in the helium rain region, the Y distribution would asymptotically settle to an exponential distribution with scale height H_r.

5.4.2. *Scheme B*

In the second scheme, we add an advective term, but do not directly find a P_1 or P_2. At each pressure and temperature point, we identify the corresponding helium mass fraction Y_{misc}, below which helium is immiscible and would rain out. To the diffusion equation (eq. 44), we add a modified advection term using $Y_{misc}(P,T)$ at every point in the planetary envelope:

$$\frac{dY}{dt} = \frac{\partial}{\partial M_r}\left\{4\pi r^2 \rho \mathcal{D}_{MLT}\left(\frac{\partial Y}{\partial r} + \frac{\max(0, Y - Y_{misc})}{\mathcal{H}_r}\right)\right\}. \quad (49)$$

Here, $\mathcal{H}_r$ is not exactly the scale height as in scheme A, but sets the scale of the helium rain region. This characteristic scale is approximately set by the ratio of $\mathcal{H}_r$ to fractional Y deficit. In addition, we ensure there is no rain below a pressure of one Mbar. The miscibility physics employed for both schemes is discussed in §6.2. Moreover, we have the capability to shift miscibility curves to taste in the way some researchers have suggested may be necessary to comport with Jupiter and Saturn (Fortney & Hubbard 2003; Püstow et al. 2016; Mankovich et al. 2016; Mankovich & Fortney 2020).

6. MICROPHYSICS

6.1. *Hydrogen-Helium Equations of State*

The evolution of gas giant planets and brown dwarfs depends on the properties of hydrogen and helium (H-He) mixtures at high pressures (Hubbard 1970; Burrows et al. 1997; Fortney & Hubbard 2003; Mankovich & Fortney 2020). Early models of brown dwarfs and giant planets used the hydrogen-helium equation of state (EOS) computed by Saumon et al. (1995). Under the "chemical picture", this model estimated the gradual ionization of hydrogen and helium with increasing pressure and temperature and relied on the volume addition law to calculate the different EOS properties for an arbitrary helium mass fraction, Y. This chemical model has been
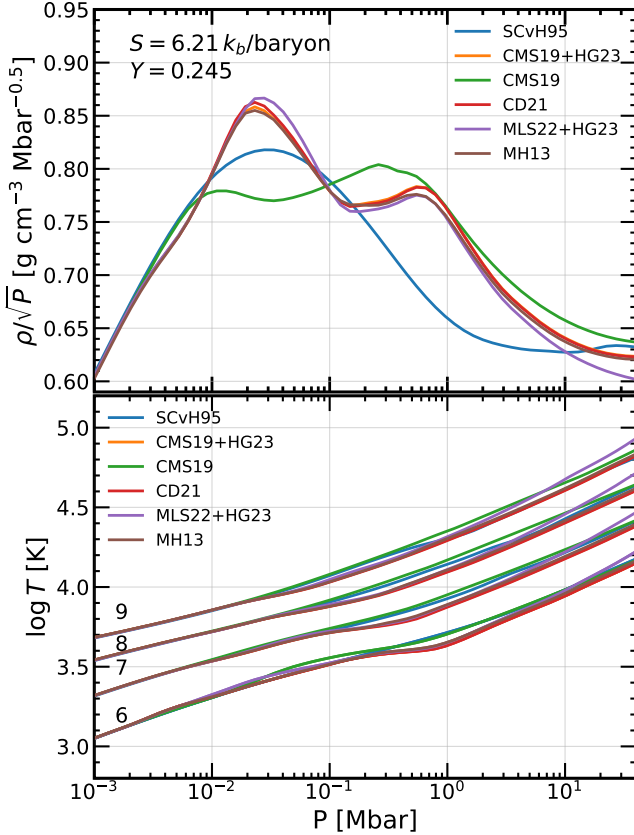
Figure 2. Reproduction of Figure 4 from Howard et al. (2023), featuring corresponding labels for helium mass fraction $Y = 0.245$, and $S = 6.21$ kb/baryon. Bottom: Adiabatic profiles at various entropy values, measured in kb/baryon units. This behavior replicates findings illustrated in Figure 10 of Militzer & Hubbard (2013) Under modest pressures of approximately 1 Mbar, non-ideal effects cause deviations from the equations of state proposed by SCvH95. Notably, these deviations occur in the same region where the demixing of hydrogen and helium is anticipated. (Figure inspired by that in Tejada Arevalo et al. (2024).)

used to evolve extra-solar giant planets, brown dwarfs, and low mass stars (Burrows et al. 1997, 2001) and to model giant planet evolution with helium rain (Fortney & Hubbard 2003; Mankovich et al. 2016). However, as reviewed by Tejada Arevalo et al. (2024), this chemical EOS model could not incorporate partial ionization for species and non-ideal interaction corrections to the H-He entropy of mixing.

Under the "physical" picture, Density Functional Theory (DFT) with Molecular Dynamics (MD) was used to obtain these non-ideal interaction terms directly. These techniques produced a more physical H-He EOS, published by Militzer & Hubbard (2013, MH13). Hubbard & Militzer (2016), Mankovich & Fortney (2020), Militzer & Hubbard (2024), and Mankovich & Fuller (2021) then

used this EOS to infer the structure and composition of Jupiter and Saturn at the present age. Nevertheless, this EOS was computed for only one helium mass fraction ($Y = 0.245$) and requires extensions to accommodate other helium mass fractions. Physical EOSes published by Chabrier et al. (2019, CMS19), Chabrier & Debras (2021, CD21), and Mazevet et al. (2022, MLS22) offer quantities that span the full range of thermodynamic space required for giant planet evolution, including a wide range of helium mass fractions, but require the use of the volume addition law (Peebles 1964; Chabrier et al. 1992) to accomplish the latter. The volume addition law is understood to be provisional and approximate and ab initio calculations for a wide range of helium fractions have yet to be performed and published.

The EOS model of CD21 incorporates the non-ideal EOS of MH13 at $Y = 0.245$. Howard et al. (2023, HG23) then calculated, using the MH13 and CD21 EOSes, these non-ideal effects for the CMS19 and the MLS22 EOSes for an arbitrary helium fraction. Currently, the CD21, CMS19, and MLS22 EOSes, with non-ideal terms calculated by HG23, are the most up-to-date models of H-He EOSes available for gas giant planet evolutionary calculations. Figure 2 compares these various equations of state along various adiabats and for a helium fraction of 0.245. These EOSes, coupled with updated H-He immiscibility curves, can be used to compute evolutionary models of Jupiter and Saturn with helium rain. APPLE allows one to employ not only the SCvH95 EOS, but also the new EOSes of MH13, CMS19, CD21, and MLS22. Importantly, APPLE can include the non-ideal entropy of mixing terms for the CMS19 and MLS22 EOSes via the EOS toolkit developed by Tejada Arevalo et al. (2024).

6.2. *Hydrogen-Helium immisciblity*

To account for the excess flux observed in Saturn identified in early evolutionary calculations, Stevenson (1975) and Pollack et al. (1977) proposed the existence of helium/hydrogen phase separation and helium rain. Early models of helium rain (Fortney & Hubbard 2003) with H-He phase separation curves calculated by Hubbard & Dewitt (1985) found that helium rain could account for the hotter effective temperatures ($T_{\rm eff}$) observed in Saturn. The first phase separation models using MD techniques (Pfaffenzeller et al. 1995) found that hydrogen-helium demixing temperatures were too cold for helium rain to exist in Jupiter or Saturn. Later DFT-MD-based demixing models for H-He mixtures by Lorenzen et al. (2009, 2011, L0911), Morales et al. (2013), and Schöttler & Redmer (2018, SR18) suggested hotter demixing temperatures at metallic hydrogen pressures. The models of L0911 and SR18 have since been

used in gas giant planet evolutionary calculations. However, several researchers concluded that these models required shifts to the demixing temperatures for helium rain to in fact occur in Jupiter and Saturn (Nettelmann et al. 2015; Püstow et al. 2016; Mankovich et al. 2016; Mankovich & Fortney 2020). Figure 3 compares examples of the various miscibility curves, along with an approximate Jupiter adiabat. As discussed in more detail in Tejada Arevalo et al. (2024), the H-He demixing temperatures remain highly uncertain at pressures relevant to gas giant planet interiors. This uncertainty is further exacerbated by the recent experiments of Brygoo et al. (2021), who observed demixing temperatures far above the model demixing temperatures of L0911 and SR18. APPLE provides options to incorporate the L0911 and SR18 demixing curves as a function of pressure and helium abundance in ways that are fully consistent with their helium fraction dependencies (§5.4). It also provides a fit to the Brygoo et al. (2021) data and temperature-offset variants of the L0911 and SR18 curves.
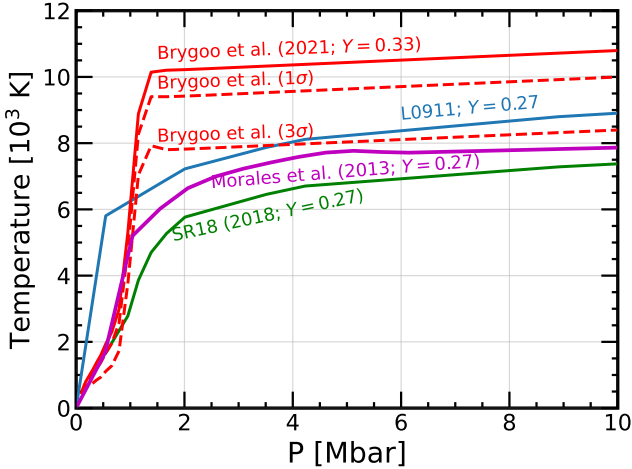
Figure 3. The various miscibility curves in T-P space are shown by different colors: Brygoo et al. (2021) (red), (Lorenzen et al. 2009, 2011) (blue), Morales et al. (2013) (purple), and Schöttler & Redmer (2018) (green). The Brygoo et al. (2021) experiments found demixing temperatures far above the recent models of SR18 and L0911, indicating that our current understanding of these miscibility curves is only loosely constrained. Note that due to the sparseness of the Brygoo et al. (2021) data, the σ error bar curves shown for them are notional. The curves are at fixed helium mass fraction ($Y = 0.27$). (Figure inspired by one found in Tejada Arevalo et al. (2024).)

6.3. *"Metal" Equations of State*

The gaseous envelopes and "solid" cores of giant planets are thought to contain "ices" and "rocks", but the proportions and actual character of such constituents in either region are unknown. APPLE provides a variety of mixtures that can be incorporated into models. For water, we use the EOS of Haldemann et al. (2020), which incorporates different phases of water by collecting and connecting water EOSes from Feistel & Wagner (2006); Journaux et al. (2020); French & Redmer (2015); Wagner & Pruß (2002); Bollengier et al. (2019), and Mazevet et al. (2019). The pure water EOS can be combined with hydrogen and helium via the volume-mixing law, accounting for the entropy of mixing terms for each species via:

$$S_{\mathrm{mix}} = S_{XY}(1 - Z) + S_{H_2O}Z + S_{\mathrm{id}}, \qquad (50)$$

where S_{XY} is the hydrogen-helium mixture entropy, S_{H_2O} the entropy of water, along with the water abundance (here denoted Z), and S_{id} is the ideal entropy of mixing. The ideal entropy of mixing of each component i of m systems is defined as

$$S_{\mathrm{id}} = k_b\left[N \ln N - \sum_{i=1}^{m} N_i \ln N_i\right]. \qquad (51)$$

This water EOS is used as our baseline for H-He-Z mixtures throughout the interior of our current models, but can easily be changed and generalized to accommodate any mixture. In cases where the H-He EOS contains non-ideal and ideal terms, like those found in the CMS19+HG23 and MLS22+HG23 EOSes, the ideal entropy of mixing of H-He is computed in advance and is then subtracted from the mixture to add the H-He-Z ideal entropy of mixing instead. This means that the H-He-Z mixture accounts for the three-component ideal entropy of mixing, but not the three-component non-ideal terms since those require ab initio mixture calculations. Currently, such mixture equations of state incorporating all interaction terms and non-ideal entropy terms are not available.

For post-perovskite and iron EOSes, APPLE incorporates those developed by Jisheng Zhang (private communication), which have been applied in rocky planet evolution models (Zhang & Rogers 2022). As a default for giant planet evolutionary calculations using APPLE, Tejada Arevalo et al. (2024) have calculated various water/ice-perovskite-iron mixture tables, but these can easily be supplemented to incorporate any materials and mixtures. In summary, in APPLE, the metal content of the envelopes is assumed to be water, while the core is assumed to be made up of a mixture of water, silicates, and iron. However, APPLE has been constructed to incorporate any mixture in either regime, as the need arises.
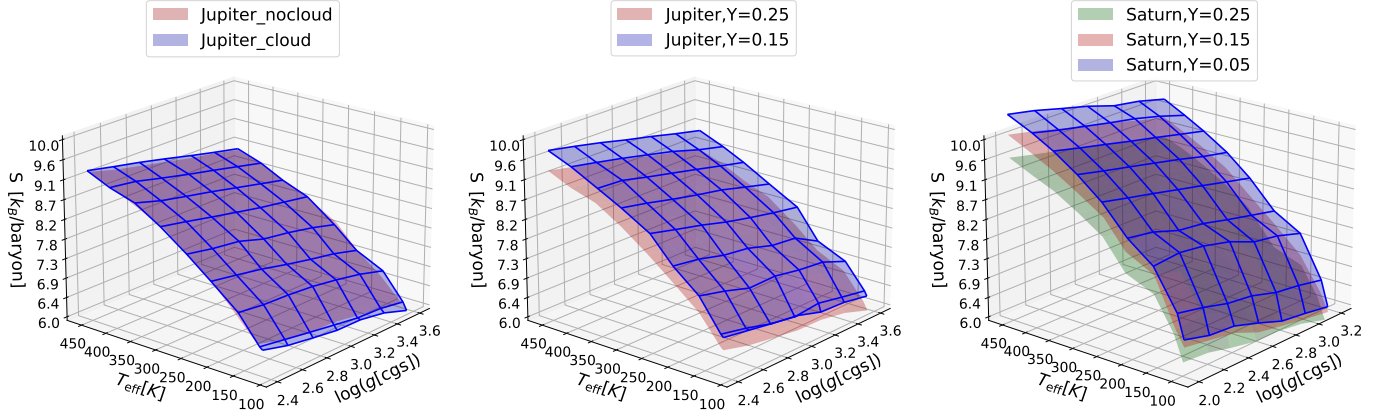
Figure 4. Effective temperature sheets for Jupiter and Saturn as a function of gravity and entropy. The left panel shows the effect of clouds in Jupiter. The middle and the right panels show the variation with helium fraction for Jupiter and Saturn, respectively. Jupiter models assume 3.16 solar metallicity and solar irradiation at a semi-major axis of 5.2 A.U., while Saturn models assume 5.0 solar metallicity and solar irradiation at a semi-major axis of 9.6 A.U.

7. ATMOSPHERES

The effects of atmospheres on giant planet cooling were investigated by Graboske et al. (1975), while Hubbard (1977) and Pollack et al. (1977) developed the first thermal evolution models of Jupiter and Saturn that coupled atmosphere boundary conditions and interior structures. Following this, Burrows et al. (1997) computed non-gray 1D atmosphere models using multi-frequency radiative transfer. These atmospheres were pre-calculated and tabulated. During an evolutionary simulation, the resulting table is interpolated to derive the internal flux temperature ($T_{\rm int}$) and surface losses. This approach is more sophisticated than commonly employed in stellar and planetary evolution and is closely equivalent to performing detailed atmosphere boundary calculations at every evolutionary timestep. The tables map the entropy (S) at the base of the radiative layer and surface gravity g to the internal brightness temperature $T_{\rm int}$ (eq. 8) necessary to evolve brown dwarfs and giant planets, including Jupiter and Saturn (Hubbard et al. 1999; Fortney & Hubbard 2003). In a similar fashion, Fortney et al. (2011) computed grids of radiative-convective model atmospheres for Jupiter, Saturn, Uranus, and Neptune over a range of $T_{\rm int}$ and g that includes the influence of stellar/solar irradiation. These models were customized to the individual characteristics of each planet, such as appropriate chemical abundances. Their boundary conditions have been utilized in numerous planetary evolutionary simulations, such as Mankovich et al. (2016) and Mankovich & Fortney (2020). However, the effect of clouds was not accounted for in these models.

More recently, in the spirit of Burrows et al. (1997), Chen et al. (2023) calculated a suite of boundary atmospheric models that include ammonia clouds with different particle sizes, irradiation, metallicity parameters, and the latest opacities (Lacy & Burrows 2023). For Jupiter evolutionary models, the fiducial cloud and irradiation parameters in Chen et al. (2023) have been calibrated to match the measured temperature structure and geometric albedo spectrum of Jupiter from *Galileo* probe data (von Zahn & Hunten 1992; Niemann et al. 1992; Young et al. 1996; Li et al. 2018) and can in principle be used for computing evolutionary models for giant exoplanets. APPLE incorporates the Chen et al. (2023) atmospheres as outer flux boundary conditions, which also allows it to generate both spectra and (for irradiated planets) reflection and Bond albedos as a function of time, but it can also incorporate the boundary conditions of Fortney et al. (2011) or those of Burrows et al. (1997) at the choice of the user. Chen et al. (2023) included various improvements to past implementations, such as updated chemistry (e.g., Lodders & Fegley 2002; Lacy & Burrows 2023), non-gray opacities (Sharp & Burrows 2007; Freedman et al. 2008), cloud formation (Burrows et al. 2006a), and the effects of stellar irradiation (Sudarsky et al. 2000; Baraffe et al. 2003; Burrows et al. 2006b; Fortney et al. 2011). The boundary condition table maps both S and g to both $T_{\rm eff}$ and $T_{\rm int}$ (which deviates from $T_{\rm eff}$ when heating from irradiation is significant). Figure 4 depicts sample tables. The atm_bc module in APPLE allows one to switch between Burrows et al. (1997), Fortney et al. (2011), and Chen et al. (2023) boundary conditions. APPLE offers the option to interpolate between purpose-built tables at a
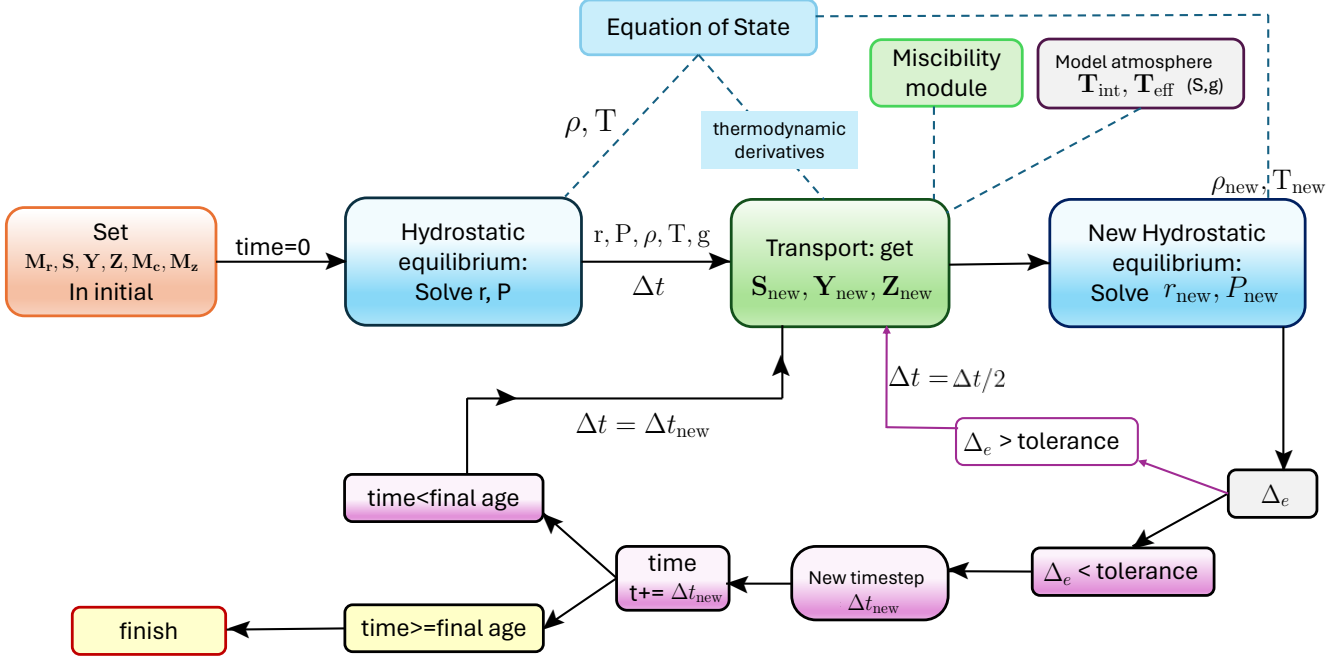
Figure 5. Flowchart of the `APPLE` code showing the different function calls. The Δ_e is calculated as the maximum of the fractional changes in density, temperature, entropy, and the helium fraction, while the tolerance is usually set to 1%.

variety of atmospheric helium abundances ($Y_{\rm atm}$). This is important in the context of significant helium depletion of the atmosphere due to helium rain. The general methodology described here for handling atmospheres is the default in `APPLE` for simulating the evolution of giant exoplanets.

8. CALCULATIONAL ALGORITHM

In addressing the structure and evolution equations 1-5, we adopt the Henyey formalism (Henyey et al. 1964), which employs the Lagrangian coordinate M_r in spherical symmetry, rather than the radius r. Consequently, all variables, including radius and density, are expressed as functions of mass coordinates and time, denoted as $r(M_r,t)$ and $\rho(M_r,t)$, respectively. Our calculations involve using an operator split technique, where we first compute the hydrostatic equilibrium for our initial conditions. Then, we advance the time and fully implicitly update the entropy, using the energy equation, and the element mass fractions, using the mixing/diffusion prescriptions (§5), after which we loop back to put the structure into hydrostatic equilibrium at the new entropies and mass fractions.

The initialization process involves setting user-defined parameters such as the total planetary mass M, core mass M_c in Earth masses, envelope heavy element mass M_z in Earth masses, initial Y_0 and Z_0 profiles, and an initial entropy (S_0) profile. We can incorporate diverse materials within the core and can employ various H-He EOSes in the envelope (Saumon et al. 1995; Chabrier

et al. 2019; Chabrier & Debras 2021). These are integrated into the hydrostatic module, which uses an iterative two-dimensional Newton-Raphson scheme for computations, i.e.

$$\vec{F}(\vec{x}+\delta\vec{x}) = \vec{F}(\vec{x}) + \frac{d\vec{F}}{d\vec{x}}\delta\vec{x} = 0 \qquad (52)$$

$$\vec{x}_{i+1} = \vec{x}_i - [J(\vec{x}_i)]^{-1}\vec{F}(\vec{x}_i) \qquad (53)$$

$$\vec{x}_{i+1} - \vec{x}_i \leq \epsilon, \qquad (54)$$

where $\vec{F}$ takes in equations 1 and 2 for the hydrostatic structure, $\vec{x} = \{r, P\}$. $\vec{J}$ is the Jacobian matrix, with components $J_{ij} = \partial F_j/\partial x_i$, and ϵ is the Newton-Raphson tolerance. The hydrostatic solver requires an initial guess for the pressure (P_g) and the radius (r_g) profiles which are obtained for the initial model at time zero using a 4th-order Runge-Kutta integration scheme. Newton's method has the advantage of *quadratic convergence*, which means it converges quickly when the initial guess is close to the solution. At each iteration, i, the density and temperature profiles are calculated from the EOS module, which has been structured to use $S, P, Y,$ and Z as independent variables.

Next, a miscibility scheme needs to be chosen. Default options are the L0911 (Lorenzen et al. 2009, 2011), SR18 (Schöttler & Redmer 2018), and Brygoo21 (Brygoo et al. 2021) miscibility curves, but any other miscibility theories can easily be incorporated, as can shifts in temperature to the default miscibility models. Under helium rain scheme A, the miscibility module returns two pres-

sure points P_1 and P_2 where the $P - T$ profile of the planet intersects the miscibility curve. If no intersection is found, the module returns `None`. Conversely, scheme B returns $Y_{\text{misc}}(P, T)$.

A small initial timestep Δt is selected before the start of the evolution. With the planet in hydrostatic equilibrium, entropy S and the element fraction Y are updated at time Δt. The helium rain algorithm is chosen using the miscibility scheme. Temperature gradients in the radiative and conductive fluxes are treated implicitly where the temperature is expanded, via

$$T_{\text{new}} = T_{\text{old}} + \left(\frac{\partial T}{\partial S}\right)_{\rho, Y} \Delta S + \left(\frac{\partial T}{\partial Y}\right)_{\rho, S} \Delta Y, \quad (55)$$

(dropping for the moment the ΔZ terms). The convective flux is expressed as an entropy gradient such that the evolution tends to make the entropy flat (in fact, slightly "superadiabatic") in regions with uniform compositions. To calculate the boundary energy flux (σT_{int}^4), T_{int} is interpolated from the atmosphere grid using the surface gravity (g) and entropy. The thermal evolution equation 4, along with the species diffusion equation 5, are discretized into algebraic equations and solved fully implicitly in time using, again, the iterative Newton-Raphson method (equations 52-54). The tolerance (ϵ) for the Newton-Raphson convergence is set at 10^{-6}. Almost all thermodynamic derivatives are treated explicitly, and evaluated using the planet profile at the current time. The exception is the derivative entering into $\mathcal{D}$ via v_{MLT} (eq. 17), which is updated every Newton-Raphson iteration. This improves numerical stability. To tackle this system of nonlinear algebraic equations, and the hydrostatic equations, we utilize a sparse matrix solver from the linear algebra package in *SciPy*.

With the new entropy S_n, and new species fractions Y_n, Z_n, a new hydrostatic equilibrium is calculated. Following this, we estimate the maximum fractional changes of S, Y, Z, ρ, T,

$$\Delta_e = \max\left(\frac{|\Delta S|}{S}, \frac{|\Delta Y|}{Y}, \frac{|\Delta Z|}{Z}, \frac{|\Delta \rho|}{\rho}, \frac{|\Delta T|}{T}\right), \quad (56)$$

and compare with the user-defined timestep tolerance. If the change is below the time tolerance, we allow the timestep to grow according to

$$\Delta t_{\text{new}} = \min(\Delta t_{\text{old}} * \min(\text{tolerance}/\Delta_e, 2), \text{max\_step}), \quad (57)$$

where max_step is chosen to be 20 Myr. If Δ_e exceeds the time tolerance, the timestep is halved and subsequent steps (i.e., the thermal and hydrostatic updates), are recalculated until $\Delta_e \leq$ tolerance. Lastly, time is advanced and compared with the planet's final age. A

complete flowchart of the code is given in Figure 5 and the outline is summarized in Algorithm 1.

Algorithm 1 Main Algorithm for `APPLE`

Input : Set initial parameters: M, M_c, M_z, tolerance, ϵ and initial values for $r_g, P_g, S_o, Y_o, Z_o, t = 0$

1 $r_o, P_o, \rho_o, T_o, g = $ hydrostatic $(r_g, P_g, S_o, Y_o, Z_o, \epsilon)$
2 Set Δt (taken to be small)
3 **while** $t \leq$ final_age **do**
4 $\quad$ Call miscibility module
5 $\quad$ Get $T_{\text{int}}(S_o, g_o)$ from atmosphere boundary condition
6 $\quad$ $S_n, Y_n, Z_n = $ transport$(r_o, P_o, \rho_o, T_o, S_o, Y_o, Z_o, T_{\text{int}}, \Delta t, \epsilon)$
7 $\quad$ $r_n, P_n, \rho_n, T_n, g = $ hydrostatic $(r_o, P_o, S_n, Y_n, Z_n, \epsilon)$
8 $\quad$ Calculate Δ_e
9 $\quad$ **if** $\Delta_e >$ tolerance **then**
10 $\quad\quad$ Repeat steps 6 and 7 with $\Delta t = \Delta t/2$
11 $\quad$ **else**
12 $\quad\quad$ Calculate new timestep: $\Delta t = \Delta t_{\text{new}}$
13 $\quad\quad$ Advance time: $t+ = \Delta t$
14 $\quad\quad$ Store all variables
15 $\quad\quad$ Set:
$\quad\quad\quad S_o = S_n$
$\quad\quad\quad T_o = T_n$
$\quad\quad\quad r_o = r_n$
$\quad\quad\quad P_o = P_n$
$\quad\quad\quad Y_o = Y_n$
$\quad\quad\quad Z_o = Z_n$
16 $\quad\quad$ **continue**
17 $\quad$ **end**
18 **end**

**Output:** Save final values

---

8.1. *Energy Conservation*

Conventionally, the total energy is the sum of the internal and gravitational potential energies. This means at any time t, we have

$$E_{\text{tot}}(t) = \int_0^{M_p} U(M_r, t) dM_r - \int_0^{M_p} \frac{GM_r}{r(M_r, t)} dM_r, \quad (58)$$

where here we have dropped for convenience the rotational kinetic energy term (associated with the last term in eq. 1). Conservation of energy means that the change in E_{tot} over time t must be compensated by the total radiation losses from the surface:

$$E_{\text{tot}}(t) - E_{\text{tot}}(0) + \int_0^t 4\pi R_p^2 \sigma T_{\text{int}}^4 dt = 0. \quad (59)$$

In our code, although we implement the `tds` form of the energy equation (eq. 4) during transport computations, we utilize equation (58) for assessing energy conservation. Across most simulations, with a time tolerance of
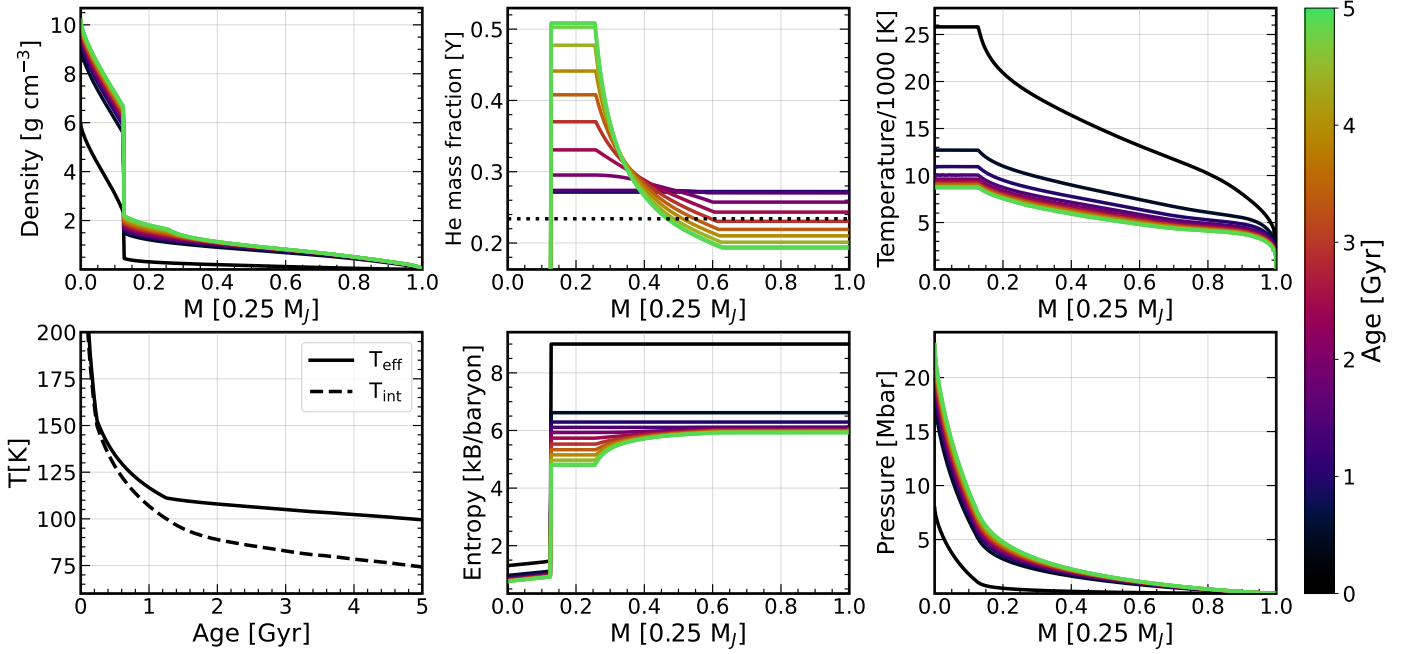
Figure 6. Evolutionary profiles for a non-rotating 0.25 M_J planet characterized by a core mass of $10 M_\oplus$, and a H-He envelope uniformly mixed with heavy elements, with a mass of $5 M_\oplus$. The CMS19+HG23 EOS is utilized for the H-He mixture, while the L0911 miscibility curve with no temperature shift is employed to model helium rain. Various parameters including density, helium mass fraction, temperature, pressure, and entropy are displayed in panels moving clockwise from the top-left to bottom-middle. The planet's effective temperature ($T_{\rm eff}$) and internal temperature ($T_{\rm int}$) are presented in the bottom-left panel. The dotted line in the top-middle panel shows the *Galileo* constraint $Y_{\rm atm} \sim 0.234$ (von Zahn et al. 1998). We have used the 5 solar metallicity Saturn atmospheric boundary condition. The color scale indicates the different ages in Gyr. Heat transport via convection uses the Schwarzschild criterion. The helium fraction in the core is zero.

1% and 500 spatial zones, we observe energy conservation of approximately 0.8% compared to the total radiation energy lost within $5-10$ Gyrs. This value improves with finer spatial resolution and stricter time tolerance settings, but we find this level of conservation adequate for our detailed simulations. We note that this quantity is rarely tracked in other extant codes, but is a useful index of code fidelity.

9. EXAMPLE SIMULATIONS

In this section, we provide example simulations for a variety of model setups and giant planets of different masses. Rotation is not included and each model incorporates a dense core, composed of 50% water ice, 33% post-perovskite, and 17% iron mixture with a total mass $M_c = 10$ Earth masses ($M_\oplus$). Surrounding this core is an H-He envelope, enriched with water ice, accounting for a heavy element mass (M_Z) of 5 $M_\oplus$ uniformly distributed in the envelope. For the water ice, we employ the AQUA EOS, and for the H-He mixture, the CMS19+HG23 is used. Note that this EOS has non-ideal entropy correction terms as incorporated by Howard et al. (2023). The initial helium mass fraction in the envelope is set at $Y = 0.272$ (Lodders 2019). It is not well understood what initial compositional and

entropy profiles arise due to planet formation (Helled & Lunine 2014; Lozovsky et al. 2017; Helled & Stevenson 2017). Therefore, for these test runs we set our initial entropy to $S_0 = 9$ k_B/baryon. This conforms to a hot-start initial condition (Marley et al. 2007; Spiegel & Burrows 2012), where the planet is puffed-up and has a radius ~ 2 times the radius of Jupiter (R_J). For the low-mass planet model tests, we use the Saturn atmospheric boundary condition to calculate the outward flux. That table is constructed for $5\times$ solar metallicity and is available for three helium fractions, i.e. 0.25, 0.15, and 0.05, in which we interpolate to derive $T_{\rm int}$ for an instantaneous outer helium fraction Y. The heavy element mass fraction, Z, is held constant in time. In all of these example models, the evolution uses our helium rain scheme B outlined in 5.4.2, using the L0911 miscibility curve with no temperature shifts. The value of the parameter $\mathcal{H}_r$ is set equal to $= 10^8$ cm. We use 500 mass zones by default. By implementing a time step tolerance of 1%, we achieve energy conservation close to 0.8% and note that minor adjustments to this tolerance do not markedly alter the outcomes. The data are saved every 20 Myr during the evolution. We emphasize that the models discussed in this section are not our preferred
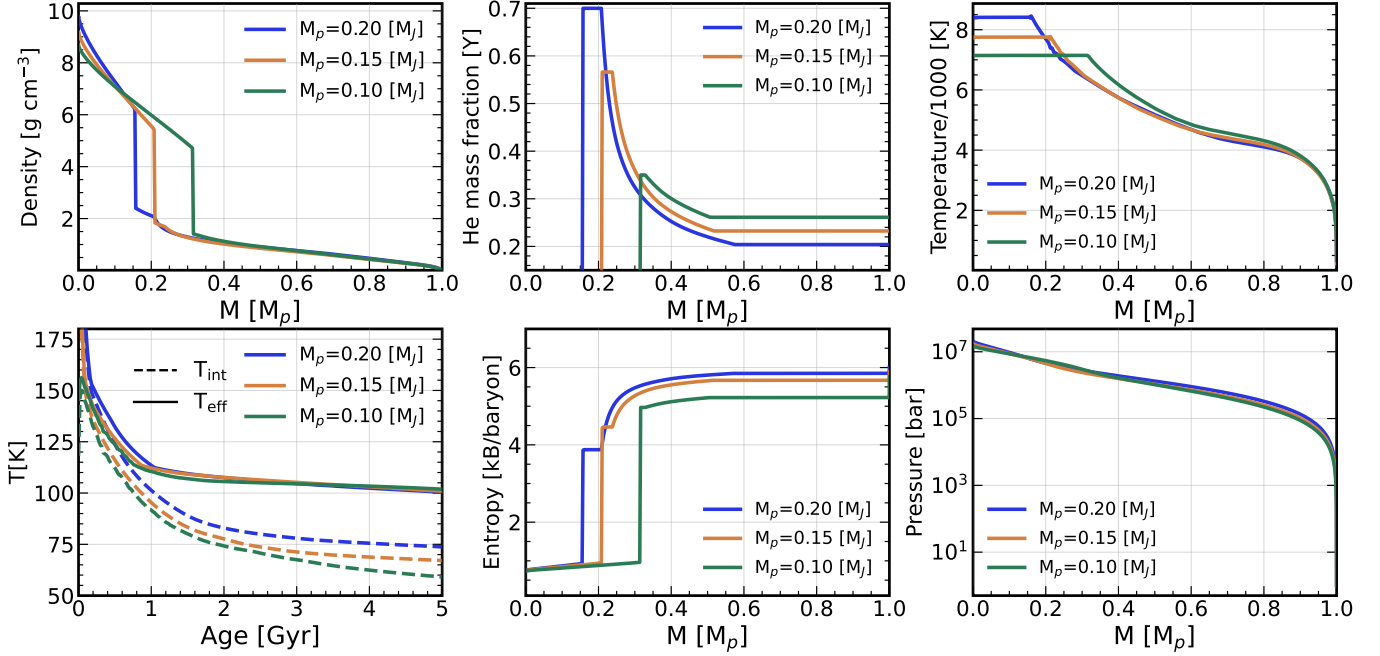
Figure 7. A comparison between different thermodynamic state variables: helium fraction, effective temperature (T_{eff}), and internal temperature (T_{int}) at the 5 Gyr mark for three distinct planet masses of $M_p = 0.2 M_J$ (blue), $M_p = 0.15 M_J$ (orange), and $M_p = 0.1 M_J$ (green). All models have $M_c = 10 M_\oplus$, and $M_z = 5 M_\oplus$. The model with $M_p = 0.2 M_J$ undergoes more helium depletion due to a larger miscibility region. The T_{eff} is, however, indistinguishable and is sensitive to the atmospheric boundary condition employed.

models for the objects studied and that we plan soon to publish these in upcoming papers.

9.1. *Evolution of Low-Mass Giant Planets*

We describe here the evolution of a model $0.25\ \mathrm{M}_J$ giant planet and assume the Schwarzschild condition for convective stability within the planet. Figure 6 shows the evolution with time of several key metrics relative to the planet's normalized mass, including density, helium mass fraction, temperature, entropy, pressure, and internal and effective temperatures. The color scale represents the planet's age in Gyrs. For these models, we embedded core masses containing roughly 12.5% of the total planetary mass. The cooling process of the planet is evident from its temperature profiles, indicating a decrease in temperature and entropy over time. Heat transfer from the core is modeled purely via conduction, assuming a conductivity $\lambda = 10^{12}$ ergs cm^{-1} s^{-1} K^{-1}. In this way, the thermal diffusion timescale in the core remains small, ensuring it remains nearly isothermal at every time step. This can be seen in the top-right panel, where the temperature profiles in the core remain flat. Rather than assuming constant temperatures in the planet's core (Baraffe et al. 2008; Lopez & Fortney 2014), we allow in this model the core and mantle to couple thermally. The pressure profiles are continuous

(bottom-right panel) with central pressure P_c reaching almost 24 Mbar at the end of our simulation.

As indicated in Figure 6, the planet's early compositional profile is homogeneous until its temperature-pressure profile intersects the L0911 miscibility curve at around 1.2 Gyr. At this point, helium starts differentiating from hydrogen, rains out, and redissolves in metallic regions at higher pressures. As a result, the Y profiles increase toward the core, and the fraction in the outer envelope drops (top-middle panel). We observe flat Y profiles below and above the demixing region due to the convective mixing of material on short time scales there, around 100 years, compared with our simulation time step of 20 million years. As previously mentioned, there is no helium diffusion into the core. This model experiences significant helium rain and its immiscibility region grows with time, as seen in previous studies (Fortney & Hubbard 2003; Püstow et al. 2016; Mankovich et al. 2016). The atmospheric helium abundance reaches $Y_{\mathrm{atm}} \sim 0.19$, while the helium fraction below the immiscibility region becomes ~ 0.5, conserving the total mass of helium. As illustrated in the bottom-middle panel, this phenomenon generates heat and results in a slowing of the decrease in the entropy of the planet's outer envelope. As a result, the greater the depletion of helium, the greater the heating effect and the greater the effect on the planet's cooling. Notably, as depicted in
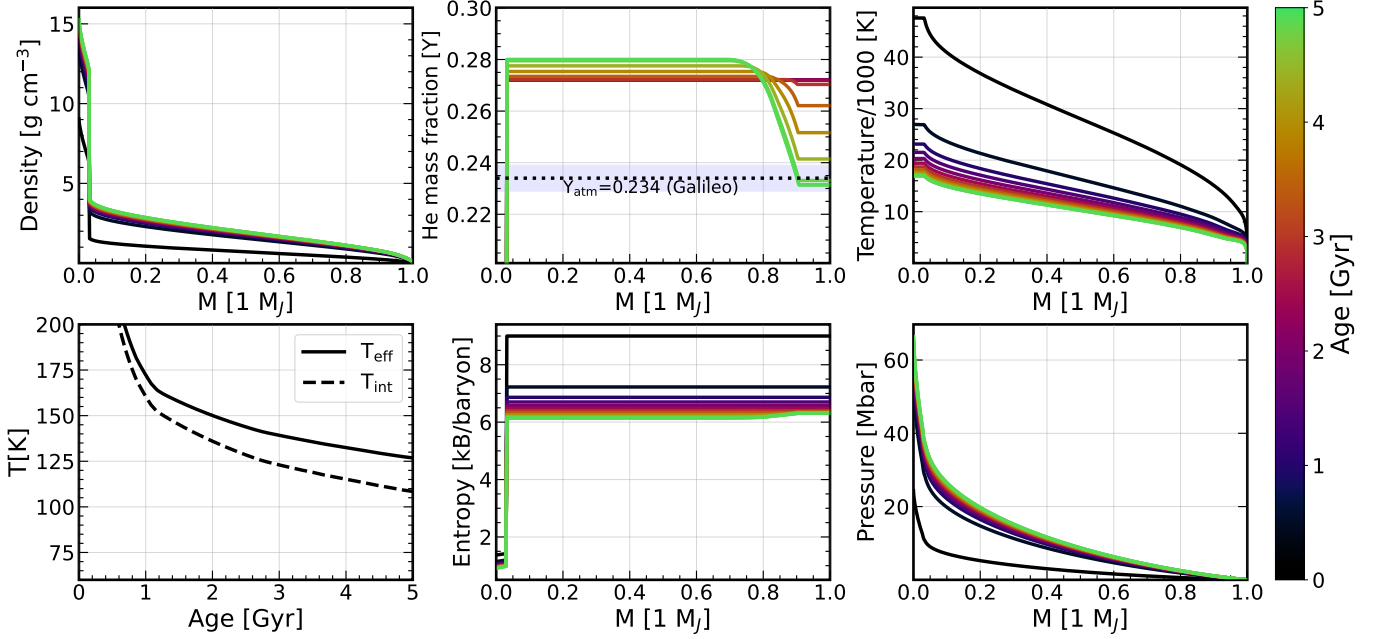
Figure 8. Same as Figure 6, but evolutionary profiles for a 1 M_J model. We use the Chen et al. (2023) atmospheric boundary condition to calculate the outward-going flux. The dotted line in the top-middle panel shows the *Galileo* constraint with the shaded region showing the uncertainty in the measurement (von Zahn et al. 1998).

the bottom-left panel, the evolution of the effective temperature ($T_{\rm eff}$) and the internal temperature ($T_{\rm int}$) over time presents an intriguing aspect. The cooling process is extended after the onset of helium rain, resulting in an effective temperature of about 100 K after 5 Gyr.

In Figure 7, we compare the evolutionary profiles at 5 Gyr for giant planets with masses of $M_p = \{0.20, 0.15, 0.10\}\, M_J$. Because M_c and M_z are kept constant, the total heavy element mass fractions differ for the different planets. Due to this, the size of the core also varies and the density jump lies at different locations across the core-envelope boundary (top-left panel). We start with different initial entropies for each planet while maintaining hot-start initial conditions with an initial planet radius of $2-3$ times R_J. Higher-mass planets exhibit sustained elevated temperatures in their cores, while the envelope remains hotter for lower-mass planets (as depicted in the top-right panel). This is due to the higher metal content by mass for our low-mass planets. Correspondingly, central pressure increases with higher M_p (as depicted in the bottom-right panel). Our simulations indicate that the core size and the extent of the immiscibility region affect the amount of helium depletion. Since lower-mass planets have narrower immiscibility regions, their Y in the deeper layers is lower and their $Y_{\rm atm}$ is higher (top middle panel). We observe significant helium depletion for the $0.2M_J$ planet, with its immiscibility region extending to the core-envelope boundary and its $Y_{\rm atm}$ reaching ~ 0.2. The evolution of $T_{\rm eff}$ and

$T_{\rm int}$ for the different masses are shown in the bottom-left panel. The impact of helium rain in extending the cooling process is evident across all models. Nevertheless, their effective temperatures become indistinguishable in the later stages of evolution. Notably, the internal temperature is lower for the lower mass planet. However, the evolution is influenced by the atmospheric boundary condition employed, which isn't custom-tailored for these specific models, but serves as a proxy to showcase the impact of a realistic representation.

9.2. *Evolution of* 1 M_J *Giant Planet*

We now discuss the evolution of an artificial Jupiter-mass object. This model also consists of a core of mass $M_c = 10 M_\oplus$ made up of the same composition described above, with $M_z = 5 M_\oplus$ in the envelope made of water-ice. We use the CMS19+HG23 EOS for modeling the H-He envelopes and the L0911 miscibility curve without any temperature shift for modeling helium-rain using scheme B. However, we lower the $\mathcal{H}_r$ to 5×10^7 cm in this model to match the *Galileo* constraint. We employ the $3.16\times$ solar metallicity Jupiter atmospheric boundary condition (Chen et al. 2023) to calculate the luminosity lost from the surface. The model atmosphere includes ammonia clouds with a particle size of 1 micron and a redistribution parameter $P_{\rm irr} = 0.5$, which redistributes between the day and night regions the intercepted solar flux originating at a distance of 5.2 A.U.
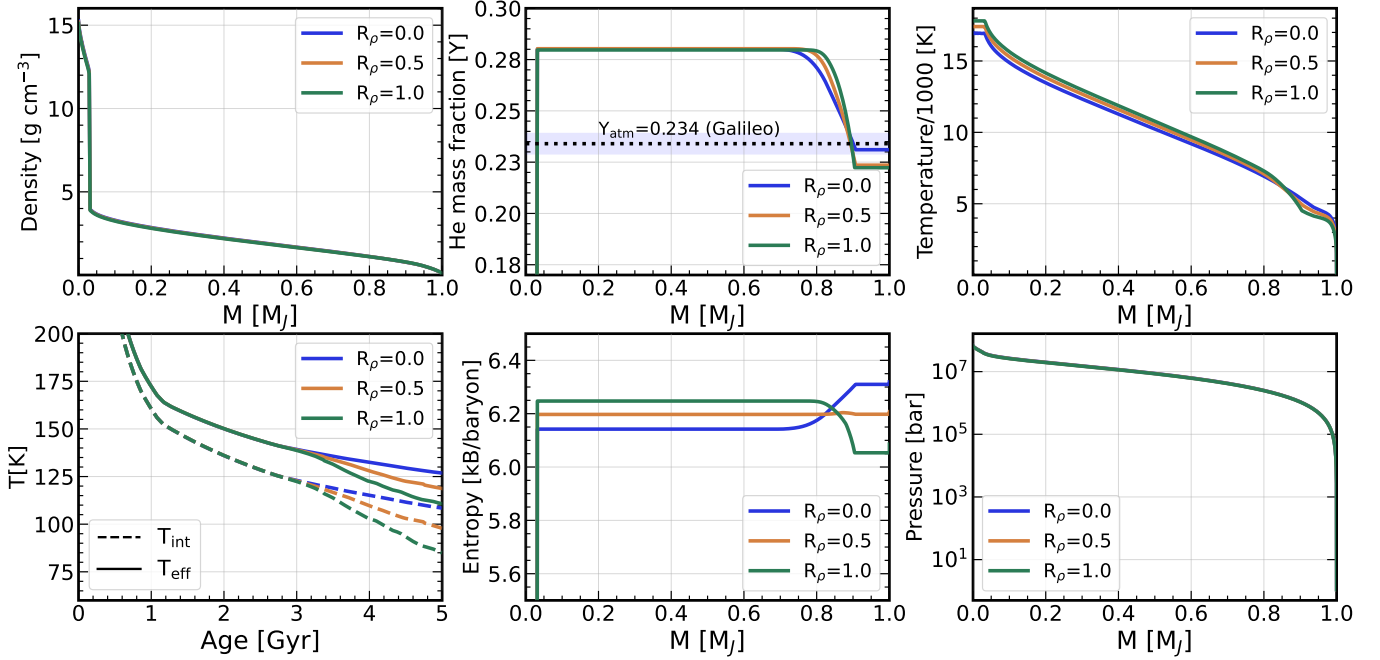
Figure 9. A comparison of the different state variables, and the effective and internal temperatures at 5 Gyr for the example $1M_J$ model with varying R_ρ parameter. The blue line corresponds to $R_\rho = 0$ (Schwarzschild criterion), the green line corresponds to $R_\rho = 1$ (Ledoux criterion), and the orange corresponds to $R_\rho = 0.5$ (crudely, semiconvection). All other model parameters are the same as in Figure 8. With helium-rain, $R_\rho = 0$ produces a hotter planet than the rest.

Figure 8 illustrates evolutionary profiles of different quantities with panels corresponding to the same variables discussed in the 0.25 M_J case. The density profile is represented in the top-left panel, where the jump marks the transition from the envelope to the core, each having a different composition. The compact core roughly makes up 3% of the planet's mass. After an initial rapid contraction phase, the planet continues to cool and the central temperature reduces from 48,000 K to 16,700 K in 5 Gyr. Concurrently, the central pressure increases to about 64 Mbar. The top-right panel displays the temperature profiles. The helium mass fraction and entropy profiles at different points in the planet's evolution are depicted in the middle top and bottom panels, respectively. Before the onset of helium rain, the planet undergoes homogeneous evolution. Around 2.4 Gyr into its evolution, the planet begins to separate into different layers, with helium-rain continuing thereafter because its $P - T$ profiles then lie below the L0911 immiscibility curve. During this period, the helium mass fraction in the atmosphere decreases, eventually reaching approximately $Y_{\rm atm} \sim 0.231$ by the 5 Gyr mark. The convective stability of the planet is assessed using the Schwarzschild criterion, indicating that the planet maintains full convection throughout, which facilitates efficient heat transport across the demixing zone. This process contributes to heating the outer envelope and

retarding the decrease in the surface entropy. The result is an entropy on the periphery of 6.31 kB/baryon, while that in the interior envelope is at 6.1 kB/baryon.

The evolution of $T_{\rm eff}$ and $T_{\rm int}$ are shown in the bottom left panel. The kink observed at 1.2 Gyr is caused by the formation of ammonia clouds at an atmospheric temperature of ~ 160 K. This prolongs the cooling of the planet which results in $T_{\rm eff} \sim 126$ K and $T_{\rm int} \sim 107$ K by the end of our simulation.

Next, depicted in Figure 9, we adjust the parameter R_ρ to study its influence on the evolutionary profiles. Here, $R_\rho = 0$ corresponds to the Schwarzschild criterion, illustrated in blue, $R_\rho = 1$ represents the Ledoux criterion, shown in green, and $R_\rho = 0.5$, shown in orange, serves to explore in a very approximate fashion the effect of efficient semiconvection. While pressure, temperature, and density profiles exhibit similarities at 5 Gyr, variations in entropy, helium fraction, and $T_{\rm eff}$ are observed. These models experience helium rain, leading to subtle differences in the atmospheric helium content towards the end, which decreases with an increase in R_ρ from 0 to 1. Specifically, the model with $R_\rho = 0$ experiences effective heat transport through the helium-rain zone, resulting in a hotter outer envelope. This can be observed by looking at the surface entropies in the bottom right panel. In contrast, employing the pseudo-semiconvection criterion or the Ledoux criterion reduces

heat transport efficiency through the helium-rain zone, causing the surface to cool more, while the interior remains hotter. The evolution of $T_{\rm eff}$ and $T_{\rm int}$ further highlights the differences in heat transport, depicted in the bottom-left panel, where a decreasing trend is observed with an increase in R_ρ, in agreement with Mankovich et al. (2016).

Collectively, these test evolutionary simulations provide a glimpse at the capabilities of APPLE. There are many parameters that can be altered to study the broad spectrum of possibilities, and we have shown here but a few examples. The ultimate goal is to identify the crucial features of giant planets and these are naturally informed by the recent measurements of the Jovian planets of our solar system. In the near future, we will apply APPLE to assess the likely range of physical characteristics that determine the evolution, or range of likely evolutionary pathways, of giant exoplanets, Jupiter, and Saturn and these investigations will be informed by the knowledge culled using *Galileo*, *Juno*, and *Cassini*. We will also be guided by theories of planet formation (Bodenheimer & Pollack 1986; Pollack et al. 1996; Alibert et al. 2005; D'Angelo et al. 2011; Mordasini et al. 2012), with one goal being to help discriminate the various birth scenarios of this important class of planet.

10. SUMMARY

With this paper, we have introduced APPLE, a new planetary evolution code purpose-built to study the evolution of giant planets. This software tool is tailored specifically to address the emerging complexities of planetary evolution revealed by recent planetary probes. Key to the development of APPLE has been the incorporation of the most current equations of state for hydrogen, helium, ices, and rock; the inclusion ice/rock cores and metals in the gaseous envelope; the embedding of conservative prescriptions for helium rain and hydrogen/helium immiscibility; the use of detailed atmosphere boundary tables (which also provide self-consistent Bond and geometric albedos and multi-frequency spectra); and options for envelope metal gradients and stably-stratified regions. The pre-calculated atmosphere tables employ the latest molecular opacities and a sophisticated spectral and atmosphere algorithm already validated over the last twenty years of exoplanet and brown dwarf research.

By integrating these advanced features from the start, APPLE will facilitate the simulation in an integrated fashion of the complex processes of giant planet evolution that have emerged to be of central importance since the revelations of *Juno*, *Cassini*, and *Galileo*. APPLE is now poised to create a new generation of giant exoplanet and Jovian planet evolutionary models and, hopefully, to elevate this fascinating and important topic to the next level of physical fidelity.

ACKNOWLEDGMENTS

APPENDIX

NUMERICAL METHODS

Practical stellar evolution codes, such as MESA (Paxton et al. 2011, 2013, 2015, 2018, 2019), Cambrdige STARS (Eggleton 1971), YREC (Demarque et al. 2008), GARSTEC (Weiss & Schlattl 2008), and CESAM (Morel & Lebreton 2008), and ASTEC (Christensen-Dalsgaard 2008) use iterative methods instead of direct integration. Within the Henyey formalism (Henyey et al. 1964), mass zones (M_r) are set in advance and are not modified during the iterations. The convergence process becomes significantly faster when the timesteps are selected to be sufficiently small. The thermodynamic variables P, ρ, T, S, and element mass fractions X_i are defined at the cell centers while the masses and the radii are defined at cell faces (see Figure 10). We use a mass grid M[4], with N+1 dimensions and follow the convention in which the indices are numbered from $k = 0$ (surface) to $k = N$ (center).

---

[4] We drop the subscript r from M_r for convenience.

HYDROSTATIC EQUILIBRIUM

In stellar and planetary evolution, it is often useful to employ log quantities. Let us also define $x = \ln r$, $y = \ln p$, and $q = \ln \rho$. With these definitions, we recast the hydrostatic equilibrium equations 1 and 2 to the following form:

$$\frac{dy}{dM} = -\frac{GM}{4\pi} \exp(-4x - y) + \frac{\Omega^2}{6\pi} \exp(-y - x) \tag{1}$$

$$\frac{dx}{dM} = \frac{1}{4\pi} \exp(-3x - q_r), \tag{2}$$

where Ω is obtained by conserving angular momentum. The finite difference scheme for the above set of equations for cells $1 \le k \le N-2$ are:

$$G_k \equiv y_{k-1} - y_k + \frac{G}{8\pi}(M_{k-1} - M_k) \exp\left(-\frac{1}{2}(y_{k-1} + y_k) - 4x_k\right) - \frac{(M_{k-1} - M_k)\Omega_k^2}{12\pi} \exp\left(-x_k - \frac{1}{2}(y_{k-1} + y_k)\right) = 0 \tag{3}$$

$$H_k \equiv x_k - x_{k+1} - \frac{1}{4\pi}(M_k - M_{k+1}) \exp\left(-\frac{3}{2}(x_k + x_{k+1}) - q_k\right) = 0. \tag{4}$$

At the boundaries, we treat the hydrostatic equations differently. At the surface $(k = 0)$,

$$G_0 \equiv \exp(y_0) - P_{\text{atm}} - \frac{GM_0}{8\pi}(M_0 - M_1) \exp(-4x_0) = 0 \tag{5}$$

$$H_0 \equiv x_0 - x_1 - \frac{1}{4\pi}(M_0 - M_1) \exp\left(-\frac{3}{2}(x_0 + x_1) - q_0\right) = 0, \tag{6}$$

while at the center $(k = N-1)$,

$$G_{N-1} \equiv \exp(y_{N-2}) - \exp(y_{N-1}) + \frac{G}{2}\left(\frac{4\pi}{3.0}\right)^{1/3} M_{N-1}^{2/3} \rho_{N-1}^{4/3} = 0 \tag{7}$$

$$H_{N-1} \equiv x_{N-1} - \frac{1}{3}\left(\ln\left[\frac{3M_{N-1}}{4\pi}\right] - q_{N-1}\right) = 0. \tag{8}$$

At $k = N$, $x_N = 0$. Thus, there are 2N unknown variables, i.e. $\{(x_0, x_1, .., x_{N-1}), (y_0, y_1, ..., y_{N-1})\}$, and 2N unknown equations $\{(G_0, G_1, .., G_{N-1}), (H_0, H_1, ..., H_{N-1})\}$. These are solved using an iterative Newton-Raphson scheme discussed in section §8.

TRANSPORT

The transport module solves equations 3, 4, and 5 simultaneously. These are time evolution equations, where n denotes the current timestep and $n-1$ denotes the previous timestep. Generally, the coefficients and the radius in these equations are treated explicitly, while any term involving S, Y, and Z is treated implicitly. The finite difference scheme for $0 \le k \le N-1$ is given by

$$E_k \equiv S_k^n - S_k^{n-1} + \sum_i \left.\frac{\partial U_k}{\partial X_i}\right|_{S,\rho} \frac{(X_i^n(k) - X_i^{n-1}(k))}{T_k^{n-1}} + \frac{\Delta t}{T_k^{n-1}(M_k - M_{k-1})}\left(4\pi r_k^2 \mathcal{F}_k^n - 4\pi r_{k-1}^2 \mathcal{F}_{k-1}^n\right) = 0 \tag{9}$$

$$D_k \equiv Y_k^n - Y_k^{n-1} + \frac{\Delta t}{M_k - M_{k-1}}\left(4\pi r_k^2 F_i^n(k) - 4\pi r_{k-1}^2 F_i^n(k-1)\right) = 0, \tag{10}$$

where F_i^n is the species flux including the diffusive and advective terms. The energy fluxes $\mathcal{F}^n$ are composed of radiation, conduction, and convection and must be implicitly treated. We expand the individual components as follows:

$$\mathcal{F}_k^{\text{cd/r}} = -\frac{\lambda_{\text{cd/r}}}{r_{k+1/2} - r_{k-1/2}}\left(T_{k+1}^n - T_k^n\right) \tag{11}$$

$$= -\frac{\lambda_{\text{cd/r}}}{r_{k+1/2} - r_{k-1/2}}\left(T_{k+1}^{n-1} + \left.\frac{\partial T}{\partial S}\right|_{\rho,Y}\Delta S_{k+1} + \left.\frac{\partial T}{\partial Y}\right|_{\rho,S}\Delta Y_{k+1} - T_k^{n-1} - \left.\frac{\partial T}{\partial S}\right|_{\rho,Y}\Delta S_k - \left.\frac{\partial T}{\partial Y}\right|_{\rho,S}\Delta Y_k\right), \tag{12}$$
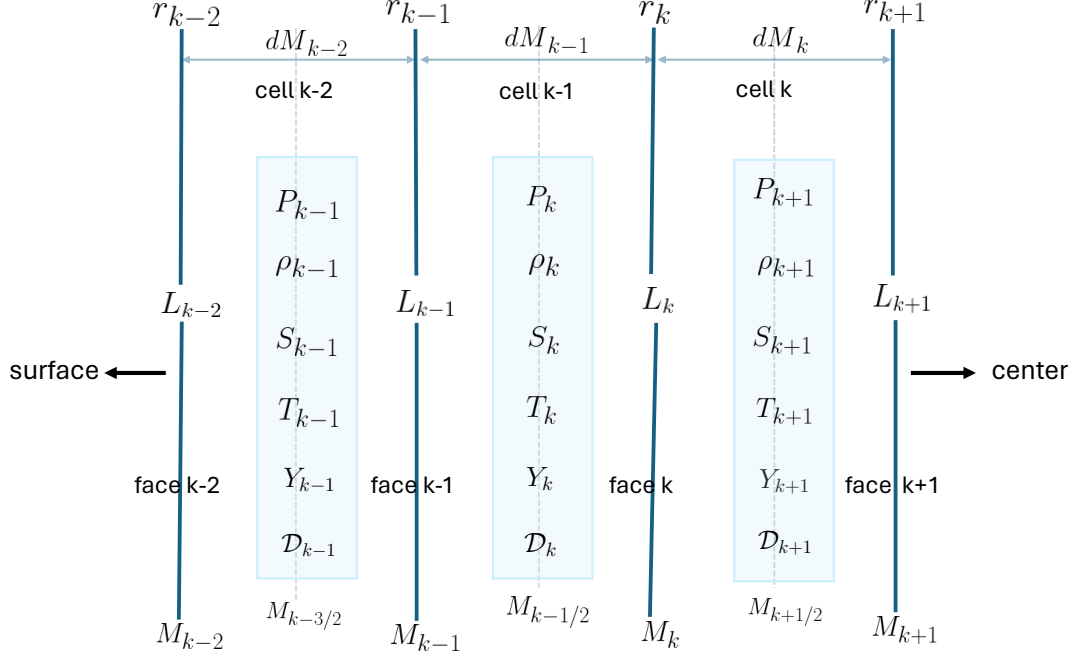
Figure 10. Finite difference grid showing locations of various thermodynamic variables and the Lagrangian coordinate M. The radius r, mass coordinate M, and the luminosities L are evaluated at cell faces, while all other quantities are evaluated at cell centers.

where cd/r stands for conduction/radiation (where we have dropped the ΔZ terms here and below for simplicity). For the convection flux, we have,

$$\mathcal{F}_k^{\mathrm{conv}} = \rho_{k+1/2}^{n-1} T_{k+1/2}^{n-1} \sqrt{\frac{gH_p^4}{32C_p}} \left[\max\left(0, -\frac{S_{k+1}^n - S_k^n}{r_{k+1/2} - r_{k-1/2}} + \left(\frac{\partial S}{\partial Y}\bigg|_{P,T}\right) \frac{Y_{k+1}^n - Y_k^n}{r_{k+1/2} - r_{k-1/2}} \right) \right]^{3/2}. \qquad (13)$$

$\mathcal{F}_{k-1}$ can be obtained by simply replacing the index k by $k-1$ in the above equations. At the center, all the fluxes go to zero automatically as $r_N = 0$. In the case of a core, the species flux at the core-envelope boundary is set to zero. At the surface, we do not allow any Y flux. However, the energy flux $\mathcal{F}_{\mathrm{surf}}$ is set by the atmosphere boundary condition and is treated implicitly,

$$\mathcal{F}_{\mathrm{surf}} = \sigma T_{\mathrm{int}}^4(n) = \sigma T_{\mathrm{int}}^4(n-1) + 4\sigma T_{\mathrm{int}}^3(n-1) \frac{\partial T_{\mathrm{int}}}{\partial S}\bigg|_0 (S_0^n - S_0^{n-1}) + 4\sigma T_{\mathrm{int}}^3(n-1) \frac{\partial T_{\mathrm{int}}}{\partial Y}\bigg|_0 (Y_0^n - Y_0^{n-1}). \qquad (14)$$

Again, there are 2N unknown equations $\{(E_0, E_1, .., E_{N-1}), (D_0, D_1, ..., D_{N-1})\}$ with 2N unknown variables $\{(S_0, S_1, .., S_{N-1}), (Y_0, Y_1, ..., Y_{N-1})\}$, which are solved simultaneously using the Newton-Raphson solver. The overall scheme is implicit and the transport sector update itself is solved in such a way that the flux into a zone is exactly equal to the flux out of the corresponding adjacent zone. In this way, energy (and in fact composition) is conserved to machine accuracy during the thermal and compositional updates. The operator splitting with the hydrostatic solve slightly breaks this (except for composition), but as shown in §8 overall energy conservation is quite good ($< 1\%$).

REFERENCES

Alibert, Y., Mordasini, C., Benz, W., & Winisdoerffer, C. 2005, A&A, 434, 343, doi: 10.1051/0004-6361:20042032

Arras, P., & Bildsten, L. 2006, ApJ, 650, 394, doi: 10.1086/506011

Bahcall, J. N., Serenelli, A. M., & Basu, S. 2006, ApJS, 165, 400, doi: 10.1086/504043

Baraffe, I., Chabrier, G., Allard, F., & Hauschildt, P. H. 1998, A&A, 337, 403, doi: 10.48550/arXiv.astro-ph/9805009

Baraffe, I., Chabrier, G., & Barman, T. 2008, A&A, 482, 315, doi: 10.1051/0004-6361:20079321

Baraffe, I., Chabrier, G., Barman, T. S., Allard, F., & Hauschildt, P. H. 2003, A&A, 402, 701, doi: 10.1051/0004-6361:20030252

Becker, A., Lorenzen, W., Fortney, J. J., et al. 2014, ApJS, 215, 21, doi: 10.1088/0067-0049/215/2/21

Berardo, D., & Cumming, A. 2017, ApJL, 846, L17, doi: 10.3847/2041-8213/aa81c0

Bodenheimer, P., & Pollack, J. B. 1986, Icarus, 67, 391, doi: 10.1016/0019-1035(86)90122-3

Böhm-Vitense, E. 1958, ZA, 46, 108

Bollengier, O., Brown, J. M., & Shaw, G. H. 2019, JChPh, 151, 054501, doi: 10.1063/1.5097179

Bolton, S. J., Lunine, J., Stevenson, D., et al. 2017a, SSRv, 213, 5, doi: 10.1007/s11214-017-0429-6

Bolton, S. J., Adriani, A., Adumitroaie, V., et al. 2017b, Science, 356, 821, doi: 10.1126/science.aal2108

Brygoo, S., Loubeyre, P., Millot, M., et al. 2021, Nature, 593, 517, doi: 10.1038/s41586-021-03516-0

Burrows, A., Hubbard, W. B., Lunine, J. I., & Liebert, J. 2001, Reviews of Modern Physics, 73, 719, doi: 10.1103/RevModPhys.73.719

Burrows, A., Saumon, D., Guillot, T., Hubbard, W. B., & Lunine, J. I. 1995, Nature, 375, 299, doi: 10.1038/375299a0

Burrows, A., Sudarsky, D., & Hubeny, I. 2006a, ApJ, 640, 1063, doi: 10.1086/500293

—. 2006b, ApJ, 650, 1140, doi: 10.1086/507269

Burrows, A., Marley, M., Hubbard, W. B., et al. 1997, ApJ, 491, 856, doi: 10.1086/305002

Campbell, J. K., & Synnott, S. P. 1985, AJ, 90, 364, doi: 10.1086/113741

Chabrier, G., & Baraffe, I. 1997, A&A, 327, 1039, doi: 10.48550/arXiv.astro-ph/9704118

Chabrier, G., & Debras, F. 2021, ApJ, 917, 6pp, doi: 10.3847/1538-4357/abfc48

Chabrier, G., Mazevet, S., & Soubiran, F. 2019, ApJ, 872, 51, doi: 10.3847/1538-4357/aaf99f

Chabrier, G., Saumon, D., Hubbard, W. B., & Lunine, J. I. 1992, ApJ, 391, 817, doi: 10.1086/171390

Chen, Y.-X., Burrows, A., Sur, A., & Arevalo, R. T. 2023, ApJ, 957, 36, doi: 10.3847/1538-4357/acf456

Christensen-Dalsgaard, J. 2008, Ap&SS, 316, 13, doi: 10.1007/s10509-007-9675-5

Debras, F., & Chabrier, G. 2019, ApJ, 872, 100, doi: 10.3847/1538-4357/aaff65

Demarque, P., Guenther, D. B., Li, L. H., Mazumdar, A., & Straka, C. W. 2008, Astrophys. Space Sci., 316, 31, doi: 10.1007/s10509-007-9698-y

Durante, D., Parisi, M., Serra, D., et al. 2020, Geophys. Res. Lett., 47, e86572, doi: 10.1029/2019GL086572

D'Angelo, G., Durisen, R. H., & Lissauer, J. J. 2011, Exoplanets; Seager, S., Ed.; University of Arizona Press: Tucson, AZ, USA, 319

Eggleton, P. P. 1971, MNRAS, 151, 351, doi: 10.1093/mnras/151.3.351

Feistel, R., & Wagner, W. 2006, Journal of Physical and Chemical Reference Data, 35, 1021, doi: 10.1063/1.2183324

Fortney, J. J., & Hubbard, W. B. 2003, Icarus, 164, 228, doi: 10.1016/S0019-1035(03)00130-1

—. 2004, ApJ, 608, 1039, doi: 10.1086/420765

Fortney, J. J., Ikoma, M., Nettelmann, N., Guillot, T., & Marley, M. S. 2011, ApJ, 729, 32, doi: 10.1088/0004-637X/729/1/32

Freedman, R. S., Marley, M. S., & Lodders, K. 2008, ApJS, 174, 504, doi: 10.1086/521793

French, M., Becker, A., Lorenzen, W., et al. 2012, ApJS, 202, 5, doi: 10.1088/0067-0049/202/1/5

French, M., & Redmer, R. 2015, PhRvB, 91, 014308, doi: 10.1103/PhysRevB.91.014308

Fuentes, J. R., Cumming, A., & Anders, E. H. 2022, Physical Review Fluids, 7, 124501, doi: 10.1103/PhysRevFluids.7.124501

Fuller, J. 2014, Icarus, 242, 283, doi: 10.1016/j.icarus.2014.08.006

Graboske, H. C., J., Pollack, J. B., Grossman, A. S., & Olness, R. J. 1975, ApJ, 199, 265, doi: 10.1086/153689

Guillot, T., Chabrier, G., Gautier, D., & Morel, P. 1995, ApJ, 450, 463, doi: 10.1086/176156

Guillot, T., Chabrier, G., Morel, P., & Gautier, D. 1994a, Icarus, 112, 354, doi: 10.1006/icar.1994.1189

Guillot, T., Gautier, D., Chabrier, G., & Mosser, B. 1994b, Icarus, 112, 337, doi: 10.1006/icar.1994.1188

Haldemann, J., Alibert, Y., Mordasini, C., & Benz, W. 2020, A&A, 643, A105, doi: 10.1051/0004-6361/202038367

Hanel, R., Conrath, B., Herath, L., Kunde, V., & Pirraglia, J. 1981, J. Geophys. Res., 86, 8705, doi: 10.1029/JA086iA10p08705

Hanel, R. A., Conrath, B. J., Kunde, V. G., Pearl, J. C., & Pirraglia, J. A. 1983, Icarus, 53, 262, doi: 10.1016/0019-1035(83)90147-1

Helled, R., & Lunine, J. 2014, MNRAS, 441, 2273, doi: 10.1093/mnras/stu516

Helled, R., & Stevenson, D. 2017, ApJL, 840, L4, doi: 10.3847/2041-8213/aa6d08

Helled, R., & Stevenson, D. J. 2024, arXiv e-prints, arXiv:2403.11657, doi: 10.48550/arXiv.2403.11657

Helled, R., Stevenson, D. J., Lunine, J. I., et al. 2022, Icarus, 378, 114937, doi: 10.1016/j.icarus.2022.114937

Henyey, L. G., Forbes, J. E., & Gould, N. L. 1964, ApJ, 139, 306, doi: 10.1086/147754

Howard, S., Guillot, T., Bazot, M., et al. 2023, A&A, 672, A33, doi: 10.1051/0004-6361/202245625

Hubbard, W. B. 1968, ApJ, 152, 745, doi: 10.1086/149591

—. 1969, ApJ, 155, 333, doi: 10.1086/149868

—. 1970, ApJ, 162, 687, doi: 10.1086/150700

—. 1977, Icarus, 30, 305, doi: 10.1016/0019-1035(77)90164-6

Hubbard, W. B., & Dewitt, H. E. 1985, ApJ, 290, 388, doi: 10.1086/162996

Hubbard, W. B., Guillot, T., Marley, M. S., et al. 1999, Planet. Space Sci., 47, 1175, doi: 10.1016/S0032-0633(99)00042-2

Hubbard, W. B., & Militzer, B. 2016, ApJ, 820, 80, doi: 10.3847/0004-637X/820/1/80

Iess, L., Militzer, B., Kaspi, Y., et al. 2019, Science, 364, aat2965, doi: 10.1126/science.aat2965

Ingersoll, A. P., Muench, G., Neugebauer, G., et al. 1975, Science, 188, 472, doi: 10.1126/science.188.4187.472

Journaux, B., Brown, J. M., Pakhomova, A., et al. 2020, Journal of Geophysical Research (Planets), 125, e06176, doi: 10.1029/2019JE006176

Kato, S. 1966, Publications of the Astronomical Society of Japan, 18

Kippenhahn, R., & Weigert, A. 1990, Stellar Structure and Evolution (Springer)

Kippenhahn, R., Weigert, A., & Weiss, A. 2013, Stellar Structure and Evolution (Springer), doi: 10.1007/978-3-642-30304-3

Labrosse, S. 2015, Physics of the Earth and Planetary Interiors, 247, 36, doi: 10.1016/j.pepi.2015.02.002

Lacy, B., & Burrows, A. 2023, ApJ, 950, 8, doi: 10.3847/1538-4357/acc8cb

Leconte, J., & Chabrier, G. 2012, A&A, 540, A20, doi: 10.1051/0004-6361/201117595

—. 2013, Nature Geoscience, 6, 347, doi: 10.1038/ngeo1791

Ledoux, P. 1947, ApJ, 105, 305, doi: 10.1086/144905

Li, L., Jiang, X., West, R. A., et al. 2018, Nature Communications, 9, 3709, doi: 10.1038/s41467-018-06107-2

Lodders, K. 2019, arXiv e-prints, arXiv:1912.00844, doi: 10.48550/arXiv.1912.00844

Lodders, K., & Fegley, B. 2002, Icarus, 155, 393, doi: 10.1006/icar.2001.6740

Lopez, E. D., & Fortney, J. J. 2014, ApJ, 792, 1, doi: 10.1088/0004-637X/792/1/1

Lorenzen, W., Holst, B., & Redmer, R. 2009, PhRvL, 102, 115701, doi: 10.1103/PhysRevLett.102.115701

—. 2011, PhRvB, 84, 235109, doi: 10.1103/PhysRevB.84.235109

Lozovsky, M., Helled, R., Rosenberg, E. D., & Bodenheimer, P. 2017, ApJ, 836, 227, doi: 10.3847/1538-4357/836/2/227

Mankovich, C., Fortney, J. J., & Moore, K. L. 2016, ApJ, 832, 113, doi: 10.3847/0004-637X/832/2/113

Mankovich, C. R., & Fortney, J. J. 2020, ApJ, 889, 51, doi: 10.3847/1538-4357/ab6210

Mankovich, C. R., & Fuller, J. 2021, Nature Astronomy, 5, 1103, doi: 10.1038/s41550-021-01448-3

Marley, M. S., Fortney, J. J., Hubickyj, O., Bodenheimer, P., & Lissauer, J. J. 2007, ApJ, 655, 541, doi: 10.1086/509759

Marley, M. S., Gelino, C., Stephens, D., Lunine, J. I., & Freedman, R. 1999, ApJ, 513, 879, doi: 10.1086/306881

Marley, M. S., Saumon, D., Visscher, C., et al. 2021, ApJ, 920, 85, doi: 10.3847/1538-4357/ac141d

Mazevet, S., Licari, A., Chabrier, G., & Potekhin, A. Y. 2019, A&A, 621, A128, doi: 10.1051/0004-6361/201833963

Mazevet, S., Licari, A., & Soubiran, F. 2022, A&A, 664, A112, doi: 10.1051/0004-6361/201935764

Militzer, B., & Hubbard, W. B. 2013, ApJ, 774, 148, doi: 10.1088/0004-637X/774/2/148

—. 2024, Icarus, 411, 115955, doi: 10.1016/j.icarus.2024.115955

Militzer, B., Hubbard, W. B., Vorberger, J., Tamblyn, I., & Bonev, S. A. 2008, ApJL, 688, L45, doi: 10.1086/594364

Militzer, B., Hubbard, W. B., Wahl, S., et al. 2022, PSJ, 3, 185, doi: 10.3847/PSJ/ac7ec8

Mirouh, G. M., Garaud, P., Stellmach, S., Traxler, A. L., & Wood, T. S. 2012, The Astrophysical Journal, 750, 61, doi: 10.1088/0004-637X/750/1/61

Moll, R., Garaud, P., & Stellmach, S. 2016, The Astrophysical Journal, 823, doi: 10.3847/0004-637X/823/1/33

Moore, K., & Garaud, P. 2016, The Astrophysical Journal, 817, 54, doi: 10.3847/0004-637X/817/1/54

Morales, M. A., Hamel, S., Caspersen, K., & Schwegler, E. 2013, PhRvB, 87, 174105, doi: 10.1103/PhysRevB.87.174105

Morales, M. A., Schwegler, E., Ceperley, D., et al. 2009, Proceedings of the National Academy of Science, 106, 1324, doi: 10.1073/pnas.0812581106

Mordasini, C., Alibert, Y., Klahr, H., & Henning, T. 2012, A&A, 547, A111, doi: 10.1051/0004-6361/201118457

Morel, P., & Lebreton, Y. 2008, Ap&SS, 316, 61, doi: 10.1007/s10509-007-9663-9

Nettelmann, N., Becker, A., Holst, B., & Redmer, R. 2012, ApJ, 750, 52, doi: 10.1088/0004-637X/750/1/52

Nettelmann, N., Fortney, J. J., Moore, K., & Mankovich, C. 2015, MNRAS, 447, 3422, doi: 10.1093/mnras/stu2634

Nettelmann, N., Holst, B., Kietzmann, A., et al. 2008, ApJ, 683, 1217, doi: 10.1086/589806

Nettelmann, N., Movshovitz, N., Ni, D., et al. 2021, PSJ, 2, 241, doi: 10.3847/PSJ/ac390a

Niemann, H. B., Harpold, D. N., Atreya, S. K., et al. 1992, SSRv, 60, 111, doi: 10.1007/BF00216852

Paxton, B., Bildsten, L., Dotter, A., et al. 2011, ApJS, 192, 3, doi: 10.1088/0067-0049/192/1/3

Paxton, B., Cantiello, M., Arras, P., et al. 2013, ApJS, 208, 4, doi: 10.1088/0067-0049/208/1/4

Paxton, B., Marchant, P., Schwab, J., et al. 2015, ApJS, 220, 15, doi: 10.1088/0067-0049/220/1/15

Paxton, B., Schwab, J., Bauer, E. B., et al. 2018, ApJS, 234, 34, doi: 10.3847/1538-4365/aaa5a8

Paxton, B., Smolec, R., Schwab, J., et al. 2019, ApJS, 243, 10, doi: 10.3847/1538-4365/ab2241

Peebles, P. J. E. 1964, ApJ, 140, 328, doi: 10.1086/147922

Peimbert, M., Luridiana, V., & Peimbert, A. 2007, ApJ, 666, 636, doi: 10.1086/520571

Pfaffenzeller, O., Hohl, D., & Ballone, P. 1995, PhRvL, 74, 2599, doi: 10.1103/PhysRevLett.74.2599

Pollack, J. B., Grossman, A. S., Moore, R., & Graboske, H. C., J. 1977, Icarus, 30, 111, doi: 10.1016/0019-1035(77)90126-9

Pollack, J. B., Hubickyj, O., Bodenheimer, P., et al. 1996, Icarus, 124, 62, doi: 10.1006/icar.1996.0190

Potekhin, A. Y. 1999, A&A, 351, 787, doi: 10.48550/arXiv.astro-ph/9909100

Preising, M., French, M., Mankovich, C., Soubiran, F., & Redmer, R. 2023, ApJS, 269, 47, doi: 10.3847/1538-4365/ad0293

Püstow, R., Nettelmann, N., Lorenzen, W., & Redmer, R. 2016, Icarus, 267, 323, doi: 10.1016/j.icarus.2015.12.009

Robinson, T. D., & Catling, D. C. 2012, ApJ, 757, 104, doi: 10.1088/0004-637X/757/1/104

Rosenblum, E., Garaud, P., Traxler, A., & Stellmach, S. 2011, The Astrophysical Journal, 731, 66, doi: 10.1088/0004-637X/731/1/66

Saumon, D., Chabrier, G., & van Horn, H. M. 1995, ApJS, 99, 713, doi: 10.1086/192204

Schöttler, M., & Redmer, R. 2018, PhRvL, 120, 115703, doi: 10.1103/PhysRevLett.120.115703

Schwarzschild, M., & Härm, R. 1958, ApJ, 128, 348, doi: 10.1086/146548

Sharp, C. M., & Burrows, A. 2007, ApJS, 168, 140, doi: 10.1086/508708

Spiegel, D. S., & Burrows, A. 2012, ApJ, 745, 174, doi: 10.1088/0004-637X/745/2/174

Spilker, L. 2019, Science, 364, 1046, doi: 10.1126/science.aat3760

Spruit, H. C. 2013, A&A, 552, 76, doi: 10.1051/0004-6361/201220575

Stevenson, D. J. 1975, PhRvB, 12, 3999, doi: 10.1103/PhysRevB.12.3999

—. 1982, Planet. Space Sci., 30, 755, doi: 10.1016/0032-0633(82)90108-8

Stevenson, D. J., & Salpeter, E. E. 1977a, ApJS, 35, 221, doi: 10.1086/190478

—. 1977b, ApJS, 35, 239, doi: 10.1086/190479

Sudarsky, D., Burrows, A., & Pinto, P. 2000, ApJ, 538, 885, doi: 10.1086/309160

Tejada Arevalo, R., Su, Y., Sur, A., & Burrows, A. 2024, arXiv e-prints, arXiv:2401.04172, doi: 10.48550/arXiv.2401.04172

Vazan, A., Helled, R., Kovetz, A., & Podolak, M. 2015, ApJ, 803, 32, doi: 10.1088/0004-637X/803/1/32

Vazan, A., Helled, R., Podolak, M., & Kovetz, A. 2016, ApJ, 829, 118, doi: 10.3847/0004-637X/829/2/118

von Zahn, U., & Hunten, D. M. 1992, SSRv, 60, 263, doi: 10.1007/BF00216857

von Zahn, U., Hunten, D. M., & Lehmacher, G. 1998, J. Geophys. Res., 103, 22815, doi: 10.1029/98JE00695

Wagner, W., & Pruß, A. 2002, Journal of Physical and Chemical Reference Data, 31, 387, doi: 10.1063/1.1461829

Wahl, S. M., Hubbard, W. B., Militzer, B., et al. 2017, Geophys. Res. Lett., 44, 4649, doi: 10.1002/2017GL073160

Walin, G. 1964, Tellus, 16, 389, doi: 10.1111/J.2153-3490.1964.TB00175.X

Weiss, A., & Schlattl, H. 2008, Ap&SS, 316, 99, doi: 10.1007/s10509-007-9606-5

Wood, T. S., Garaud, P., & Stellmach, S. 2013, The Astrophysical Journal, 768, 157, doi: 10.1088/0004-637X/768/2/157

Young, R. E., Smith, M. A., & Sobeck, C. K. 1996, Science, 272, 837, doi: 10.1126/science.272.5263.837

Zaghoo, M., & Silvera, I. F. 2017, Proceedings of the National Academy of Science, 114, 11873, doi: 10.1073/pnas.1707918114

Zaussinger, F., & Spruit, H. C. 2013, A&A, 554, 119, doi: 10.1051/0004-6361/201220573

Zhang, J., & Rogers, L. A. 2022, ApJ, 938, 131,
   doi: 10.3847/1538-4357/ac8e65